

The scale-dependent signature of primordial non-Gaussianity in the large-scale structure of cosmic reionization

Anson D’Aloisio^{1*}, Jun Zhang^{2,1}, Paul R. Shapiro¹, and Yi Mao^{3,4,1}

¹*Department of Astronomy and Texas Cosmology Center, University of Texas, Austin, TX 78712, USA*

²*Department of Physics, Shanghai Jiao Tong University, Shanghai 200240, China*

³*CNRS, UPMC Univ Paris 06, Institut d’Astrophysique de Paris, UMR7095, 98 bis, boulevard Arago, F-75014, Paris, France*

⁴*Sorbonne Universités, Institut Lagrange de Paris (ILP), 98 bis, boulevard Arago, F-75014 Paris, France*

24 March 2021

ABSTRACT

The rise of large-scale structure in the universe depends upon the statistical distribution of initial density fluctuations generated by inflation. While the simplest models of inflation predict an almost perfectly Gaussian distribution, more-general models predict primordial deviations from Gaussianity that observations might yet be sensitive enough to detect. Recent measurements of the Cosmic Microwave Background (CMB) temperature anisotropy bispectrum by the *Planck* collaboration have significantly tightened observational limits on the level of primordial non-Gaussianity (PNG) in the Universe, but they are still far from the level predicted by the simplest models of inflation. Probing levels of PNG below CMB sensitivities will require other methods, such as searching for the statistical imprint of PNG on the clustering of galactic halos. During the cosmic epoch of reionization (EoR), the first stars and galaxies released radiation into the intergalactic medium (IGM) that created ionized patches whose large-scale geometry and evolution reflected the underlying abundance and large-scale clustering of the star-forming galaxies. This statistical connection between ionized patches in the IGM and galactic halos suggests that observations of reionization may provide another means of constraining PNG. We employ the linear perturbation theory of reionization and semi-analytic models based on the excursion-set formalism to model the effects of PNG on the EoR. We quantify the effects of PNG on the large-scale structure of reionization by deriving the ionized density bias, i.e. the ratio of the ionized atomic to total matter overdensities in Fourier space, at small wavenumber. Just as previous studies found that PNG creates a scale-dependent signature in the halo bias, so, too, we find a scale-dependent signature in the ionized density bias. Our results, which differ significantly from previous attempts in the literature to characterize this PNG signature, will be applied elsewhere to predict its observable consequences, e.g. in the cosmic 21cm background.

Key words: cosmology: theory, large-scale structure of the Universe, inflation, reionization, first stars, galaxies: statistics

1 INTRODUCTION

Observational probes of the epoch of reionization (EoR) are of great interest not only because they promise to yield new information on primordial galaxies, and the effects of their radiation backgrounds on the inter-galactic medium (IGM); these probes may some day deliver a wealth of cosmological information as well. The power spectrum of redshifted 21cm

brightness temperature fluctuations from the EoR is a notable example with great potential for cosmological application. Theoretical investigations to date have mainly focused on exploiting the separation of the matter power spectrum from the influence of astrophysical uncertainties in the EoR, which according to linear perturbation theory is made possible by anisotropy from peculiar velocity in the neutral hydrogen gas (Barkana & Loeb 2005). The possibility of this clean separation has stimulated a broad literature on the topic of constraining cosmology with future 21cm surveys

* Email: anson@astro.as.utexas.edu

[e.g. see Furlanetto et al. (2006) and references therein. Also see Shapiro et al. (2013) for a recent re-examination of this technique].

One topic currently at the forefront of research in cosmology is the possibility that the initial conditions for structure formation were not perfectly Gaussian. While the simplest inflationary models – the canonical single-field slow-roll models – predict an almost perfectly Gaussian distribution of initial fluctuations, more general inflationary models predict significant deviations from Gaussianity that observations might yet be sensitive enough to detect. There is therefore great interest in developing new ways to measure primordial non-Gaussianity (PNG) since its detection (or non-detection) would have profound implications for inflationary theory.

Perfectly Gaussian initial conditions can be entirely characterized by the power spectrum of initial density fluctuations, while PNG is characterized by higher-order statistics. The lowest-order statistic that can distinguish Gaussian from non-Gaussian primordial fluctuations is the 3-point correlation function, or equivalently, its Fourier transform – the bispectrum. In general since the bispectrum is zero for the Gaussian case, we can write it as

$$B_{\Phi}(k_1, k_2, k_3) = f_{\text{NL}} F(k_1, k_2, k_3) \quad (1)$$

where $F(k_1, k_2, k_3)$ is a function only of the magnitudes of the wavevectors of any three perturbation modes, $\mathbf{k}_{1,2,3}$ (assuming translational and rotational invariance), f_{NL} is a dimensionless parameter which indicates the level of departure from Gaussianity, called the “non-linearity parameter” (Gangui et al. 1994; Wang & Kamionkowski 2000; Komatsu & Spergel 2001; Babich et al. 2004), and Φ is the Bardeen potential fluctuation in the matter-dominated epoch. The primordial spectra generated by inflationary models vary considerably from one model to the next and can be quite complicated. Observational efforts have therefore focused on phenomenological templates which capture the dominant shapes, or functional dependences on wavenumber, of the spectra generated by wide classes of inflationary models.

An important example is the so-called “local” template, in which $\Phi(\mathbf{r})$ is obtained from a quadratic transformation of the local Gaussian fluctuation field, $\phi(\mathbf{r})$, according to¹

$$\Phi(\mathbf{r}) = \phi(\mathbf{r}) + f_{\text{NL}}^{\text{local}} [\phi(\mathbf{r})^2 - \langle \phi^2(\mathbf{r}) \rangle], \quad (2)$$

where $\langle \rangle$ refers to an average over all space (Hodges et al. 1990; Kofman et al. 1991; Salopek & Bond 1990; Gangui et al. 1994; Verde et al. 2000; Wang & Kamionkowski 2000; Komatsu & Spergel 2001). To first order in $f_{\text{NL}}^{\text{local}}$, equation (2) gives a primordial bispectrum of the following form²:

$$B_{\Phi}^{\text{local}}(k_1, k_2, k_3) = 2f_{\text{NL}}^{\text{local}} [P_{\phi}(k_1)P_{\phi}(k_2) + P_{\phi}(k_1)P_{\phi}(k_3) + P_{\phi}(k_2)P_{\phi}(k_3)], \quad (3)$$

where $P_{\phi}(k)$ the power spectrum of the Gaussian potential, defined by $\langle \phi(\mathbf{k})\phi(\mathbf{k}') \rangle \equiv (2\pi)^3 P_{\phi}(k)\delta_D(\mathbf{k} + \mathbf{k}')$. This local template is important in the phenomenology of PNG, since all single-field models of inflation with standard³ assumptions predict $f_{\text{NL}}^{\text{local}} = (5/12)(1 - n_s) \approx 0.016$, where $n_s = 0.96$ is the spectral index of the primordial power spectrum (Acquaviva et al. 2003; Maldacena 2003; Creminelli & Zaldarriaga 2004; Seery & Lidsey 2005; Chen et al. 2007; Cheung et al. 2008). Being able to detect or limit $f_{\text{NL}}^{\text{local}}$ at such a small level would therefore be an important test of single-field models. On the other hand, other more-general models of inflation exist which predict larger $f_{\text{NL}}^{\text{local}}$, so it is also possible to exclude or restrict such models by limiting $f_{\text{NL}}^{\text{local}}$ (Henceforth, we shall remove the label “local” from f_{NL} and mean $f_{\text{NL}}^{\text{local}}$ unless otherwise specified).

Observational constraints have been placed on the local template by finding the range of allowed amplitudes, expressed in terms of f_{NL} . For example, CMB anisotropy measurements by the *Wilkinson Microwave Anisotropy Probe* nine-year data analysis (WMAP9) find a 95% confidence limit of $-3 < f_{\text{NL}} < 77$ (Bennett et al. 2012). Newer CMB anisotropy results based upon the first 15 months of data from the *Planck* satellite mission are reported to yield $f_{\text{NL}} = 2.7 \pm 5.8$ [68% confidence limit error bars, Ade et al. (2013)]. This result from the highly sensitive all-sky CMB anisotropy experiment of *Planck* may be close to the limit which can be achieved by measurement of the CMB bispectrum alone (Komatsu & Spergel 2001; Babich & Zaldarriaga 2004). To confirm these limits and probe f_{NL} further, it is necessary to consider other methods.

Correlation statistics of the CMB temperature anisotropy directly probe the initial fluctuations while they are still in the linear regime. However, PNG also has potentially observable effects on the large-scale structure that develops as the initial fluctuations grow to the highly non-linear point of forming halos (see e.g. Desjacques & Seljak 2010a, and references therein). For example, since non-Gaussianity to first order adds a skewness to the distribution function of filtered initial density fluctuations, it can significantly impact the abundance of the rarest and most massive halos (e.g. Matarrese et al. 2000; Verde et al. 2001; Grossi et al. 2007; Lo Verde et al. 2008; Grossi et al. 2009; Valageas 2010; Lo Verde & Smith 2011; Desjacques & Seljak 2010b), or of low-density cosmic voids (Kamionkowski et al. 2009; D’Amico et al. 2011), both of

(2), as it can also be generated in a number of models that do not involve the latter (see footnote 34 in Komatsu et al. 2011, for example). It is nonetheless customary to refer to this form of the bispectrum as the local template.

³ By “standard” assumptions, we mean that the curvature perturbation is initially in the Bunch-Davies state, and that there is no super-horizon evolution of the curvature perturbation of a non-tractor solution. See e.g. Agullo & Parker (2011), Ganc (2011), Ganc & Komatsu (2012), Agullo & Shandera (2012), Dey & Paban (2012), Dey et al. (2012), Carney et al. (2012), Namjoo et al. (2013), and Chen et al. (2013) for models which relax these assumptions.

¹ There are two conventions for equation (2) in the literature: 1) The CMB convention in which Φ is evaluated in the matter-dominated epoch, and 2) The large-scale structure convention in which Φ is linearly extrapolated to the present day. These two conventions result in different normalizations of the non-linearity parameter, $f_{\text{NL}}^{\text{local}}(\text{LSS}) \approx 1.3 f_{\text{NL}}^{\text{local}}(\text{CMB})$. Here and throughout the rest of the paper, we use the CMB convention.

² The bispectrum in equation (3) is more general than equation

which originate from the tails of the density distribution. PNG can also leave a strong signature in the halo bias, i.e. the ratio in Fourier space of the fractional halo number overdensity to the fractional matter overdensity, by introducing a scale-dependence which originates from coupling between large and small scales modes in the initial non-Gaussian distribution (Dalal et al. 2008; Matarrese & Verde 2008; Afshordi & Tolley 2008). For the local template in equation (3), this halo bias has been found to depart significantly from the Gaussian expectation by a correction term that approaches the form $\Delta b(k) \propto f_{\text{NL}}(b_{\text{G}} - 1)/k^2$ in the small- k limit, where b_{G} is the expected Gaussian bias (for recent analytical derivations, see e.g. Desjacques et al. 2011b; Smith et al. 2012; Adshead et al. 2012; D’Aloisio et al. 2012; Yokoyama & Matsubara 2012). Based upon this assumed k^{-2} scale-dependence of $b(k)$, Giannantonio et al. (2013) recently constrained f_{NL} to be in the range $-37 < f_{\text{NL}} < 25$ (95% limit in their most conservative analysis) using both the large-scale clustering of massive galaxies and the integrated Sachs-Wolfe effect [see also Slosar et al. (2008), Xia et al. (2010), Xia et al. (2010), Xia et al. (2011) and Ross et al. (2013) for previous constraints based on the large-scale clustering of galaxies].

Fluctuations in the density of neutral and ionized hydrogen in the IGM during the EoR created by the energy released by the first stars and galaxies presents another opportunity to observe the difference between Gaussian and non-Gaussian initial conditions. During this cosmological phase, which ended at $z > 6$, before the universe was a billion years old, expanding ionized patches of the IGM were created wherever galactic halos formed to fuel their growth, so the large-scale structure of this patchiness was correlated with that of the halos. The connection between patchiness and halo clustering introduces a new kind of bias, the *ionized density bias*, i.e. ratio of the fractional overdensity of intergalactic H II to the fractional total matter overdensity, which can also reflect the difference caused by PNG. The theory of this ionized density bias, however, is dependent not only on the clustering of halos, but on the further complications of galaxy formation and radiative transfer which determine: (i) How much and what kind of ionizing radiation is released by galactic halos of different masses, (ii) How the radiation ionizes the surrounding IGM, and (iii) How that process feeds back on the ability of galactic halos to form stars and release more ionizing radiation. For galaxies to form stars, they must collapse and accrete the baryonic component of the IGM along with the dark matter that dominates the halo mass, and then they must make these baryons gravitationally unstable and self-gravitating within the halos, by radiatively cooling the gas below the halo virial temperature. A general picture of how this process unfolded in the Λ CDM universe is the following.

The first stellar sources of reionization likely formed through radiative cooling from collisional excitation of rotational-vibrational energy levels of H_2 molecules, within halos with masses between $M \sim 10^5 - 10^8 M_{\odot}$, and virial temperatures $T_{\text{vir}} \lesssim 10^4$ K - the so-called minihalos. However, this early period of star formation ($z \gtrsim 15$) is thought to have been quenched by a corresponding rise in the UV background, since the H_2 molecules needed for efficient cooling in minihalos were easily photo-dissociated by UV photons in the Lyman-Werner bands of H_2 between 11.2 and 13.6

eV (Haiman et al. 2000). Halos in this mass range would also have been suppressed as sources of ionizing radiation if they formed in places where the IGM was already ionized. The gas pressure of the ionized IGM, which is heated to $\sim 10^4$ K by photoionization, opposes baryonic gravitational collapse into minihalos, a phenomenon sometimes referred to as “Jeans filtering” (Shapiro et al. 1994), and pre-existing minihalos would also lose their baryonic content to photoevaporation by the ionizing radiation inside IGM H II regions (Shapiro et al. 2004).

Halos with $T_{\text{vir}} \gtrsim 10^4$ K, on the other hand, could radiatively cool their gas through collisional excitation of atomic hydrogen. These are the so-called atomic cooling halos (ACHs). This minimum T_{vir} for ACHs corresponds to a minimum halo-mass scale of roughly $M_{\text{min}} \sim 10^8 M_{\odot}$. In fact, like minihalos, even ACHs with masses below the Jeans-filtering scale ($M \sim 10^9 M_{\odot}$) may have been susceptible to negative feedback from IGM photo-heating if they formed within already ionized regions. These low-mass ACHs (“LMACHS”) may also not have been massive enough to overcome the IGM pressure forces which act to prevent the accretion of inter-galactic gas – the fuel of star formation [see e.g. Iliiev et al. (2007) and references therein]. The precise boundary between LMACHS and the high-mass ACHs (“HMACHS”) which are massive enough to be unaffected by Jeans filtering is still uncertain. Regardless of the astrophysical uncertainties in the theory, reionization was likely driven to completion by galaxies in halos that were massive enough to be rare and highly biased at the relevant redshifts ($z \gtrsim 6$). It is therefore natural to expect characteristic differences between EoR models with Gaussian and non-Gaussian initial conditions, and for these differences to lead to new observational signatures of PNG.

There has already been some work on the theory of reionization in the context of PNG. Crociani et al. (2009) calculated the effects of the modified ACH abundance due to PNG on the reionization history and the mean integrated electron scattering optical depth, τ_{es} , of the IGM. Tashiro & Sugiyama (2012) investigated how the modified ACH abundance can impact the number count of ionized bubbles observed in future maps of the brightness temperature of the redshifted 21cm background from the EoR, which they suggest as a potential probe of f_{NL} . Chongchitnan & Silk (2012) found that the effects of PNG on nonlinear biasing of minihalos significantly increases the root-mean-square (RMS) of fluctuations in the 21cm brightness temperature during the EoR. If minihalos are able to maintain their reservoirs of neutral hydrogen throughout the EoR, Chongchitnan & Silk (2012) claim, their contribution to the 21cm RMS may allow detection of $f_{\text{NL}} = \mathcal{O}(1)$ by next-generation radio telescopes like the Square Kilometer Array (SKA). The possibility to detect PNG by measuring the power spectrum of brightness temperature fluctuations in the 21cm background from the EoR was considered by Joudaki et al. (2011) (henceforth JDFKS). They reported a scale-dependent signature in the 21cm power spectrum for PNG which is absent in the Gaussian case. This scale-dependent signature is related to that known already for the underlying galactic halos, as expected since the latter are the sources of reionization.

JDFKS modeled reionization by semi-numeral simulations using the SimFast21 code (Santos et al. 2010), modi-

fied to take account of local PNG. This method builds upon the analytical approximation introduced by Furlanetto et al. (2004) in which reionization is statistically assumed to occur in some region when it has collapsed a large enough fraction of its mass to ionize all the atoms in that region. The collapsed fraction in the model of Furlanetto et al. (2004) is computed analytically by an application of the extended Press-Schechter approximation, sometimes referred to as the excursion-set model (ESM) (Bond et al. 1991; Lacey & Cole 1993). We shall refer to this analytical approximation, which applies the excursion-set formalism to model reionization statistically, as the excursion-set model of reionization (ESMR). The semi-numerical SimFast21 simulations go beyond the statistical approach of the ESMR by creating a 3D realization of the initial density fluctuations on a cubic mesh in a finite comoving volume prior to reionization, and extrapolating them forward in time by linear theory (the Zel’dovich approximation), to produce an evolving 3D map of the ionization field over time.

JDFKS defined a statistical quantity they called the “bias of ionized regions,” which could be used to predict the 21cm power spectrum in the small- k limit for a given reionization model in terms of the power spectrum of the underlying matter density fluctuations. In that limit, the matter-density fluctuations are linear and the effect of PNG allowed by existing constraints is negligible. The JDFKS bias quantity is $\hat{b}_x(k) = (1/\bar{x}_H)\sqrt{P_{xx}(k)/P_{\delta\delta}(k)}$, where \bar{x}_H is the mean neutral fraction, and $P_{xx}(k)$ and $P_{\delta\delta}(k)$ are the power spectra of the ionized fraction and matter density fluctuation fields respectively, i.e. $\langle\tilde{x}(\mathbf{k})\tilde{x}(\mathbf{k}')\rangle = (2\pi)^3P_{xx}(k)\delta_D(\mathbf{k}+\mathbf{k}')$, and $\langle\tilde{\delta}(\mathbf{k})\tilde{\delta}(\mathbf{k}')\rangle = (2\pi)^3P_{\delta\delta}(k)\delta_D(\mathbf{k}+\mathbf{k}')$, where δ_D is the Dirac Delta function. Using their simulated maps of the ionization field for cases with and without local PNG, JDFKS found that \hat{b}_x has a strong k -dependence in the non-Gaussian simulations, while b_x is k -independent in the Gaussian simulations on large enough scales. Much like prior studies of the halo bias, JDFKS found they could fit $\hat{b}_x^{\text{NG}}(k)$ from a given non-Gaussian simulation, as a function of \hat{b}_x^{G} from the corresponding Gaussian simulation, using a simple fitting formula in which $[\hat{b}_x^{\text{NG}}(k) - \hat{b}_x^{\text{G}}]$ scales as k^{-2} in the small- k limit. Since this scale-dependent correction for PNG was found to be proportional to f_{NL} as well, a measurement of the 21cm power spectrum at small k might enable a determination of the value of f_{NL} . Indeed, JDFKS used their fitting formula to predict that the SKA and Murchison Widefield Array (MWA) surveys could detect $f_{\text{NL}} \sim 50$ and ~ 100 respectively. Tashiro & Ho (2012) subsequently used the JDFKS fitting formula again to explore the constraining power of the cross-correlation between CMB temperature anisotropies and 21cm fluctuations on f_{NL} .

We are interested here in the general problem of predicting the signatures of PNG in the observable properties of the EoR. For this purpose, a more fundamental quantity is the *ionized density bias*, the ratio of the ionized atomic to total matter overdensities in Fourier space, $b_{\rho\text{HII}}(k) \equiv \tilde{\delta}_{\rho\text{HII}}(k)/\tilde{\delta}(k)$, where $\tilde{\delta}_{\rho\text{HII}}(k)$ is the Fourier transform of the contrast in the ionized hydrogen mass density, $\delta_{\rho\text{HII}} \equiv \rho_{\text{HII}}/\bar{\rho}_{\text{HII}} - 1$. Our goal here is to derive this ionized density bias, $b_{\rho\text{HII}}^{\text{NG}}$, for reionization models with PNG and relate it to the corresponding quantity for the Gaussian case, $b_{\rho\text{HII}}^{\text{G}}$. Along the way, we will also derive the related bias parameter \hat{b}_x defined by JDFKS for which they have

reported the fitting formula described above. As we shall discuss, we find significant differences between our derived expression and their fitting formula.

The methodology of our work is as follows: (i) We extend the analytical excursion-set model of reionization (ESMR) of Furlanetto et al. (2004) to include non-Gaussian initial conditions with general bispectra. This extension is made possible by the derivation of the non-Gaussian collapsed fraction in D’Aloisio et al. (2012) [see also Adshead et al. (2012) for a similar but independent calculation]. (ii) We use our extension of the ESMR to derive, for the first time, expressions for the scale-independent and -dependent contributions to the non-Gaussian ionized density bias, which apply to PNG with general bispectra. (iii) We test our derived expressions against more fundamental numerical calculations of the ionized density bias using the linear perturbation theory of reionization (LPTR) developed by Zhang et al. (2007), in which the linearized ionization rate and radiative transfer equations are solved in the long-wavelength limit for the perturbations to the ionized density field. This approach is ideally suited to the problem at hand since it directly employs the relevant physics equations governing the ionization state of the IGM and is expected to be most accurate on the large scales of interest (Zhang et al. 2007). The LPTR provides a powerful and computationally cheaper alternative to fully non-linear cosmological radiative transfer simulations, which at the present day are prohibitively expensive in this context, since they would have to both resolve scales down to the smallest galactic halos responsible for reionization, *and* be large enough, approaching $\sim 1 \text{ Gpc}^3$ in volume, to capture the mode-coupling effects of PNG responsible for the scale-dependent halo bias. (iv) Finally, we derive the JDFKS bias parameter from first principles using our non-Gaussian extension of the ESMR. The significant differences we find between our result and the JDFKS fitting formula, which we also confirm using the LPTR, will lead to our revision of their forecasted 21cm power spectrum constraints on f_{NL} – the topic of a follow-up paper to this work (Mao et al. 2013).

The remainder of this paper is organized as follows. In §2, we present basic definitions, our non-Gaussian extension of the analytical ESMR, and our expressions for the scale-independent and -dependent non-Gaussian ionized density bias. In §3, we summarize the LPTR formalism. In §4 we present numerical results from both the ESMR and the LPTR as well as comparisons between these two approaches. In §5 we derive our ESMR prediction for the JDFKS \hat{b}_x parameter, and discuss our differences from their fitting formula. Finally, we offer concluding remarks in §6.

In the plots presented below, we use a fiducial ΛCDM cosmology with parameters $\Omega_m = 0.28$, $\Omega_\Lambda = 0.72$, $\Omega_b = 0.046$, $H_0 = 100h \text{ km s}^{-1} \text{ Mpc}^{-1}$ (with $h = 0.7$), $n_s = 0.96$ and $\sigma_8 = 0.82$, consistent with WMAP7 constraints (Komatsu et al. 2011). We also employ the linear matter power spectrum of Eisenstein & Hu (1999). Although the expressions we derive apply to PNG with general bispectra, we use the above local template to generate all plots in the remainder of this paper. All distances are reported in comoving units unless otherwise stated.

2 ANALYTICAL MODEL OF THE IONIZED DENSITY BIAS

2.1 Basic definitions

Let $\rho_m(\mathbf{r}, z)$ be the total matter density at location \mathbf{r} and redshift z . We define the matter density contrast,

$$\delta(\mathbf{r}, z) \equiv \frac{\rho_m(\mathbf{r}, z)}{\bar{\rho}_m} - 1, \quad (4)$$

where $\bar{\rho}_m$ denotes the mean matter density.

Similarly, let $\rho_{\text{HI}}(\mathbf{r}, z)$ and $\rho_{\text{HII}}(\mathbf{r}, z)$ denote the mass densities of neutral and ionized hydrogen respectively, and let $\rho_{\text{H}}(\mathbf{r}, z) = \rho_{\text{HI}}(\mathbf{r}, z) + \rho_{\text{HII}}(\mathbf{r}, z)$ denote the total hydrogen mass density. We will from here on refer to $\rho_{\text{HII}}(\mathbf{r}, z)$ as the *ionized density*. We define the ionized density contrast as

$$\delta_{\rho_{\text{HII}}}(\mathbf{r}, z) \equiv \frac{\rho_{\text{HII}}(\mathbf{r}, z)}{\bar{\rho}_{\text{HII}}(z)} - 1, \quad (5)$$

where $\bar{\rho}_{\text{HII}}(z)$ is the mean ionized density at redshift z . The central quantity that we will use in this work to quantify the impact of PNG on the large-scale structure of reionization is the *ionized density bias*,

$$b_{\rho_{\text{HII}}}(k, z) \equiv \frac{\tilde{\delta}_{\rho_{\text{HII}}}(k, z)}{\tilde{\delta}(k, z)}, \quad (6)$$

where $\tilde{\delta}(k, z)$ and $\tilde{\delta}_{\rho_{\text{HII}}}(k, z)$ are the Fourier transforms of the matter and ionized density contrasts respectively. We now discuss how the ionized density bias is related to other quantities sometimes used in the literature.

Let $x_i(\mathbf{r}, z) \equiv \rho_{\text{HII}}(\mathbf{r}, z)/\rho_{\text{H}}(\mathbf{r}, z)$ denote the ionized fraction, and let $\delta_x(\mathbf{r}, z)$ denote the ionized fraction contrast,

$$\delta_x(\mathbf{r}, z) = \frac{x_i(\mathbf{r}, z)}{\bar{x}_i(z)} - 1, \quad (7)$$

where $\bar{x}_i(z)$ is the spatially averaged ionized fraction at redshift z . On large scales ($k \ll 1$), the ionized density bias is related to the *ionized fraction bias*,

$$b_x(k, z) \equiv \frac{\tilde{\delta}_x(k, z)}{\tilde{\delta}(k, z)}, \quad (8)$$

through the definition of the ionized fraction smoothed on scale R , $x_i(R, \mathbf{r}, z) \equiv \int d^3\mathbf{r}' W(|\mathbf{r}' - \mathbf{r}|, R) \rho_{\text{HII}}(\mathbf{r}', z)/\rho_{\text{H}}(\mathbf{r}', z)$, where $W(|\mathbf{r}' - \mathbf{r}|, R)$ is a spherically symmetric filter with characteristic cut-off scale R . If the smoothing scale is large, then the above equation for $x_i(R, \mathbf{r}, z)$ yields the leading-order relation, $\tilde{\delta}_x(k, z) + \tilde{\delta}(k, z) = \tilde{\delta}_{\rho_{\text{HII}}}(k, z)$, in the limit of $k \ll 1$, where we have assumed that the total hydrogen density fluctuations faithfully trace dark matter fluctuations on large scales. Hence, the ionized density bias is related to the ionized fraction bias for small k through

$$b_x(k, z) = b_{\rho_{\text{HII}}}(k, z) - 1. \quad (9)$$

Equation (9) can be used to transform the results for $b_{\rho_{\text{HII}}}$

presented in this paper, which are always restricted to the small- k regime, to b_x as needed.

Consider a spherical region with radius R . Let $f_{\text{coll}}(\mathbf{r}, M_{\text{min}}, R, z)$ be the fraction of mass within that region contained in halos with masses above some threshold M_{min} , i.e. the collapsed fraction. At times, we will consider the contrast in the collapsed fraction,

$$\delta_{f_{\text{coll}}}(\mathbf{r}, M_{\text{min}}, R, z) \equiv \frac{f_{\text{coll}}(\mathbf{r}, M_{\text{min}}, R, z)}{\bar{f}_{\text{coll}}(M_{\text{min}}, z)} - 1, \quad (10)$$

where $\bar{f}_{\text{coll}}(M_{\text{min}}, z)$ is the mean collapsed fraction at z , and a corresponding bias parameter,

$$b_{f_{\text{coll}}}(k, M_{\text{min}}, z) \equiv \frac{\tilde{\delta}_{f_{\text{coll}}}(k, M_{\text{min}}, z)}{\tilde{\delta}(k, z)}, \quad (11)$$

where the dependence on R has been dropped under the assumption of $k \ll 2\pi/R$.

2.2 Generalizing the excursion-set model of reionization (ESMR) to include PNG

In this section we extend the ESMR of Furlanetto et al. (2004) for Gaussian initial conditions to include PNG with general bispectra, and use it to derive expressions for the Gaussian and non-Gaussian ionized density bias parameters. These expressions will provide analytical expectations against which to compare the numerical LPTR results presented in §4.

2.2.1 General Principles of the ESMR

The basic postulate of the ESMR is that the local ionized fraction within a spherical volume with radius R is proportional to the number of ionizing photons produced within that volume or, equivalently, the local collapsed fraction of mass in luminous sources,

$$x_i(M_{\text{min}}, R, z) = \zeta_{\text{ESMR}} f_{\text{coll}}(M_{\text{min}}, R, z). \quad (12)$$

Here, the ζ_{ESMR} parameter accounts for the efficiency of this mass in releasing ionizing photons into the IGM (note that the condition of a fully ionized volume implies $f_{\text{coll}} \geq \zeta_{\text{ESMR}}^{-1}$). Rather than try to compute this parameter from first principles, we will treat it as a free parameter. When numerically evaluating our results in §4, we will fix the value of ζ_{ESMR} by specifying the electron scattering optical depth for the model. For simplicity, we assume that ACHs provide the only sources of ionizing radiation throughout reionization (see §6 for a discussion of the limitations of this assumption). The minimum $T_{\text{vir}} \gtrsim 10^4$ K criterion for ACHs roughly corresponds to a minimum halo mass of

$$M_{\text{min}} \approx 1.3 \times 10^7 M_{\odot} \left(\frac{T_{\text{vir}}}{10^4 \text{K}} \right)^{3/2} \left(\frac{1+z}{21} \right)^{-3/2} \left(\frac{\Omega_m}{0.3} \right)^{-1/2} \left(\frac{h}{0.7} \right)^{-1} \left(\frac{\mu_{\text{mol}}}{1.22} \right)^{-3/2}, \quad (13)$$

where μ_{mol} is the mean molecular weight of the gas (see e.g. Haiman & Holder 2003).

2.2.2 Gaussian initial conditions

Consider a spherical region with initial comoving radius R , containing mass $M \approx \bar{\rho}_m 4\pi R^3/3$. In models with Gaussian initial conditions, the excursion set expression for the fraction of mass within this comoving volume that will end up in ACHs at redshift z is ⁴

$$f_{\text{coll}}^{\text{G}}(M_{\text{min}}, R, z) = \text{erfc} \left[\frac{\delta_c - \delta_R(z)}{\sqrt{2[S_{\text{min}}(z) - S_R(z)]}} \right], \quad (14)$$

where $\delta_c \approx 1.686$ is the critical density in the spherical collapse model (in an Einstein-de Sitter universe),

$$\delta_R(z) = D(z) \int d^3\mathbf{r}' W(|\mathbf{r} - \mathbf{r}'|, R) \delta(\mathbf{r}', z=0) \quad (15)$$

is the density contrast, smoothed on scale R with the coordinate-space top-hat filter function, linearly extrapolated⁵ to the epoch z , with variance

$$S_R(z) \equiv \sigma_R^2 = \langle \delta_R^2 \rangle = \int \frac{d^3\mathbf{k}}{(2\pi)^3} \mathcal{M}_R^2(k, z) P_{\Phi}(k), \quad (16)$$

and $S_{\text{min}}(z)$ is the variance of density fluctuations smoothed on scale $R_{\text{min}} = (3M_{\text{min}}/4\pi\bar{\rho}_m)^{1/3}$. Above, $D(z)$ is the linear growth factor normalized to unity at $z=0$, and we have written S_R in terms of the power spectrum of the primordial potential fluctuation, P_{Φ} , and the factor $\mathcal{M}_R(k, z)$

$$\mathcal{M}_R(k, z) \equiv \frac{2}{3} \frac{k^2 \mathcal{T}(k) D(z)}{\Omega_m H_0^2} g(0) \tilde{W}(k, R), \quad (17)$$

between the potential and the smoothed density contrast in the cosmological Poisson equation in the synchronous-comoving gauge. Here, $g(0) = (1+z_i)^{-1} D^{-1}(z_i)$, where z_i corresponds to the initial epoch, i.e. the limit of large redshift, is the linear growth factor of the potential normalized to unity in the matter dominated epoch, evaluated at the present day [$g(0) \approx 0.76$ in our fiducial cosmology], and $\mathcal{T}(k)$ is the matter transfer function normalized to unity on large scales.

2.2.3 Extension to non-Gaussian initial conditions

PNG complicates the analytical calculation of the collapsed fraction considerably because the additional correlations quantified in the three-point correlation function (and in general higher-order correlation functions) make the excursion set random walks non-Markovian. D'Aloisio et al.

⁴ Strictly speaking, equation (14) applies in the case of Gaussian initial conditions *and* a sharp k -space filtering function. Under these conditions, the stochastic evolution of excursion set trajectories is Markovian, and fully tractable analytically. The use of the coordinate space top-hat filter necessitates more sophisticated analytical techniques resulting in correction terms to equation (14). For simplicity, we neglect these terms here.

⁵ In contrast to D'Aloisio et al. (2012), we do not adopt the usual convention in which the density field is linearly extrapolated all the way to the present day. The convention we adopt in the current work, where the density field is linearly extrapolated to the epoch of interest, makes the redshift dependence in many of the summarized expressions more transparent.

(2012) applied the non-Markovian extension⁶ of the excursion set formalism of Maggiore & Riotto (2010a,b,c) to calculate the collapsed fraction perturbatively [see also Adshear et al. (2012) for a similar but independent calculation]. We adopt equation (33) of D'Aloisio et al. (2012) for the collapsed fraction of ACHs,

$$f_{\text{coll}}^{\text{NG}}(M_{\text{min}}, R, z) = f_{\text{coll}}^{\text{G}} + \Delta f_{\text{coll}}^{\text{NG}}, \quad (18)$$

where the non-Gaussian correction is⁷

$$\begin{aligned} \Delta f_{\text{coll}}^{\text{NG}}(M_{\text{min}}, R, z) &= \frac{\mathcal{A}}{3} \left(\frac{\delta_c - \delta_R}{S_{\text{min}} - S_R} - \frac{1}{\delta_c - \delta_R} \right) \frac{\partial f_{\text{coll}}^{\text{G}}}{\partial S_{\text{min}}} \\ &+ \frac{\mathcal{B}}{S_R} \left[\delta_c - (\delta_c - \delta_R) \coth \left(\frac{\delta_c^2 - \delta_c \delta_R}{S_R} \right) \right] \frac{\partial f_{\text{coll}}^{\text{G}}}{\partial S_{\text{min}}} \\ &+ \mathcal{C} \cdot \frac{S_{\text{min}} - S_R}{S_R^2 (\delta_c - \delta_R)} \left\{ \delta_R^2 - S_R \right. \\ &\left. - 2(\delta_c^2 - \delta_c \delta_R) \left[\coth \left(\frac{\delta_c^2 - \delta_c \delta_R}{S_R} \right) - 1 \right] \right\} \frac{\partial f_{\text{coll}}^{\text{G}}}{\partial S_{\text{min}}}, \end{aligned} \quad (19)$$

with

$$\frac{\partial f_{\text{coll}}^{\text{G}}}{\partial S_{\text{min}}} = \frac{(\delta_c - \delta_R)}{\sqrt{2\pi}(S_{\text{min}} - S_R)^{3/2}} \exp \left[-\frac{(\delta_c - \delta_R)^2}{2(S_{\text{min}} - S_R)} \right]. \quad (20)$$

The mode coupling effects of PNG between small and large scales are encoded in the functions,

$$\mathcal{A} \equiv \langle \delta_{\text{min}}^3 \rangle - \langle \delta_R^3 \rangle + 3 \langle \delta_R^2 \delta_{\text{min}} \rangle - 3 \langle \delta_R \delta_{\text{min}}^2 \rangle \quad (21)$$

$$\mathcal{B} \equiv \langle \delta_R^3 \rangle + \langle \delta_R \delta_{\text{min}}^2 \rangle - 2 \langle \delta_R^2 \delta_{\text{min}} \rangle \quad (22)$$

$$\mathcal{C} \equiv \langle \delta_R^2 \delta_{\text{min}} \rangle - \langle \delta_R^3 \rangle, \quad (23)$$

(where $\delta_{\text{min}} \equiv \delta_{R=R_{\text{min}}}$) containing the three-point correlation functions⁸ of the smoothed, linearly extrapolated den-

⁶ See also Paranjape & Sheth (2012); Paranjape et al. (2012); Musso & Paranjape (2012); Musso & Sheth (2012); Musso et al. (2012) for other works on non-Markovian extensions of the excursion-set formalism.

⁷ Here we use the leading-order non-Gaussian correction to the collapsed fraction of D'Aloisio et al. (2012). They showed that this expression is consistent with the previously obtained non-Gaussian halo bias (Desjacques et al. 2011b), which is in good agreement with results from N-body simulations at low redshifts (Desjacques et al. 2011a). D'Aloisio et al. (2012) also obtained a next-to-leading order non-Gaussian correction which alters the collapsed fraction by a few percent. For simplicity, we neglect this correction term here.

⁸ It is technically the *connected* two- and three-point correlation functions that appear in the above ESMR expressions. However, since $\langle \delta \rangle = 0$, the connected two- and three-point correlation functions are equal to the full two- and three-point correlation functions (see e.g. Cooray & Sheth 2002). We therefore drop the distinction here.

sity field,

$$\langle \delta_{R_1} \delta_{R_2} \delta_{R_3} \rangle = \int \frac{d^3 \mathbf{k}_1}{(2\pi)^3} \frac{d^3 \mathbf{k}_2}{(2\pi)^3} B_{\Phi}(k_1, k_2, k_3) \mathcal{M}_{R_1}(k_1, z) \mathcal{M}_{R_2}(k_2, z) \mathcal{M}_{R_3}(k_3, z), \quad (24)$$

where $k_3 = \sqrt{k_1^2 + k_2^2 + 2\mathbf{k}_1 \cdot \mathbf{k}_2}$. Our non-Gaussian extension of the ESMR is achieved by plugging equation (18) into equation (12).

2.3 Ionized density bias from the ESMR

2.3.1 Gaussian initial conditions

We compute the ionized density bias in essentially the same way as D’Aloisio et al. (2012) computed the halo bias⁹. The first step is to write down the ionized fraction contrast, equation (7). Assuming Gaussian initial conditions, we find

$$\delta_x = \frac{f_{\text{coll}}^G}{f_{\text{coll},0}^G} - 1, \quad (25)$$

where the subscript, 0, in the denominator denotes the global mean collapsed fraction, i.e. evaluation in the limit of $\delta_R \rightarrow 0$ and $S_R \rightarrow 0$. We then plug in equation (14) and Taylor expand δ_x in δ_R about $\delta_R = 0$ in the limit of $S_R \rightarrow 0$. This procedure yields the leading-order relationship between the ionized fraction contrast and the initial matter contrast in the unevolved density field – the so-called Lagrangian ionized fraction bias. In order to relate this to the Eulerian bias defined in equation (8), which relates the ionized fraction contrast to the evolved matter density contrast, we adopt the spherical collapse model as in Mo & White (1996). In this model, the initial mass contained within the unevolved (i.e. Lagrangian) region is conserved, so the fraction of ionized mass in the evolved (i.e. Eulerian) region at z is equal to the fraction of the initial mass that will end up ionized at z . Moreover, in the large-scale limit, the evolved matter contrast is to first-order equal to the linearly extrapolated initial contrast. The large-scale Lagrangian and Eulerian b_x are therefore equivalent in this framework. As a final step, we convert b_x to $b_{\rho_{\text{HII}}}$ using equation (9) to obtain

$$b_{\rho_{\text{HII}}}^G = 1 + \frac{2}{\delta_c} \frac{\partial \ln f_{\text{coll},0}^G}{\partial \ln S_{\text{min}}}. \quad (26)$$

Hence, the ESMR predicts that the large-scale ionized density bias is scale-independent in models with Gaussian initial conditions, with an amplitude given by equation (26).

⁹ For Gaussian initial conditions, see also McQuinn et al. (2005) and Alvarez et al. (2006). McQuinn et al. (2005) calculated the bias of the overdensity of H II bubble counts with respect to the underlying matter density field in the standard ESMR approach. Alvarez et al. (2006) calculated both the collapsed fraction bias and the ionized fraction bias – the latter with their own model of reionization.

2.3.2 Scale-dependent ionized density bias from non-Gaussian initial conditions

Here we shall derive the ionized density bias $b_{\rho_{\text{HII}}}^{\text{NG}}$ for non-Gaussian initial conditions. For comparison with the Gaussian bias, we will write $b_{\rho_{\text{HII}}}^{\text{NG}}$ as follows:

$$b_{\rho_{\text{HII}}}^{\text{NG}} = b_{\rho_{\text{HII}}}^G + \Delta b_{\rho_{\text{HII}}}^{(i)} + \Delta b_{\rho_{\text{HII}}}^{(d)}. \quad (27)$$

where the labels “i” and “d” refer to scale-independent and scale-dependent corrections respectively. Before proceeding we make some key simplifications. Since our goal here is to compute the large-scale ionized density bias, where we will ultimately take the limit of $|\delta_R| \ll 1$ and $S_R \ll 1$, we can recast equation (19) in the much simplified form,

$$\begin{aligned} \Delta f_{\text{coll}}^{\text{NG}} &= \frac{\langle \delta_{\text{min}}^3 \rangle - 3\langle \delta_{\text{min}}^2 \delta_R \rangle}{3} \\ &\times \left(\frac{\delta_c - \delta_R}{S_{\text{min}} - S_R} - \frac{1}{\delta_c - \delta_R} \right) \frac{\partial f_{\text{coll}}^G}{\partial S_{\text{min}}} \\ &+ \frac{\langle \delta_{\text{min}}^2 \delta_R \rangle}{S_R} \left[\delta_c - (\delta_c - \delta_R) \coth \left(\frac{\delta_c^2 - \delta_c \delta_R}{S_R} \right) \right] \frac{\partial f_{\text{coll}}^G}{\partial S_{\text{min}}}. \end{aligned} \quad (28)$$

Additionally, we will require the mean non-Gaussian collapsed fraction, for which $\delta_R \rightarrow 0$ and $S_R \rightarrow 0$. In this limit, equations (18) and (28) simplify to

$$f_{\text{coll},0}^{\text{NG}} = f_{\text{coll},0}^G + \Delta f_{\text{coll},0}^{\text{NG}} \quad (29)$$

and

$$\Delta f_{\text{coll},0}^{\text{NG}} = \frac{\langle \delta_{\text{min}}^3 \rangle}{3} \left(\frac{\delta_c}{S_{\text{min}}} - \frac{1}{\delta_c} \right) \frac{\partial f_{\text{coll},0}^G}{\partial S_{\text{min}}}, \quad (30)$$

respectively.

As before, we write down the ionized fraction contrast,

$$\delta_x = \left(\frac{f_{\text{coll}}^G}{f_{\text{coll},0}^G} - 1 \right) - \frac{f_{\text{coll}}^G \Delta f_{\text{coll},0}^{\text{NG}}}{\left(f_{\text{coll},0}^G \right)^2} + \frac{\Delta f_{\text{coll}}^{\text{NG}}}{f_{\text{coll},0}^G}. \quad (31)$$

Like the analogous expression for the halo bias [see equation (57) of D’Aloisio et al. (2012)], this equation contains both scale-independent and -dependent contributions to the ionized density bias. We give technical details of our derivation in the appendix and summarize the main results here. The first term on the right-hand side of equation (31) gives the Gaussian term from the last section, equation (26). The terms from equation (28) with $\langle \delta_{\text{min}}^3 \rangle$ contribute a scale-independent correction from PNG to the bias, whereas one of the terms with $\langle \delta_{\text{min}}^2 \delta_R \rangle$ yields a non-zero scale-dependent correction. The scale-independent correction is given by

$$\begin{aligned} \Delta b_{\rho_{\text{HII}}}^{(i)} &= -\frac{\mathcal{S}_{\text{min}}^{(3)}}{6} S_{\text{min}} \left(b_{\rho_{\text{HII}}}^G - 1 \right) \left[\frac{3\delta_c S_{\text{min}} - \delta_c^3}{S_{\text{min}}^2} \right. \\ &\quad \left. + \left(b_{\rho_{\text{HII}}}^G - 1 \right) \left(\frac{\delta_c^2}{S_{\text{min}}} - 1 \right) \right], \end{aligned} \quad (32)$$

where $\mathcal{S}_{\text{min}}^{(3)} \equiv \langle \delta_{\text{min}}^3 \rangle / S_{\text{min}}^2$ denotes the skewness of density fluctuations smoothed on the M_{min} scale. The scale-dependent correction is given by

$$\Delta b_{\rho_{\text{HII}}}^{(d)}(k) = 2\delta_c \left(b_{\rho_{\text{HII}}}^{\text{G}} - 1 \right) \frac{\mathcal{F}_{\text{min}}^{(3)}(k)}{\mathcal{M}_{\text{min}}(k)}, \quad (33)$$

where the form factor is

$$\mathcal{F}_R^{(3)}(k) = \frac{1}{4S_R P_\phi(k)} \int \frac{d^3 \mathbf{k}_1}{(2\pi)^3} \quad (34)$$

$$\times \mathcal{M}_R(k_1, z) \mathcal{M}_R(q, z) B_\Phi(k, k_1, q),$$

with $q = \sqrt{k^2 + k_1^2 + 2\mathbf{k} \cdot \mathbf{k}_1}$ (as before, we use the shorthand notation $\mathcal{F}_{\text{min}}^{(3)} \equiv \mathcal{F}_{R=R_{\text{min}}}^{(3)}$ and $\mathcal{M}_{\text{min}} \equiv \mathcal{M}_{R=R_{\text{min}}}$). The scale-dependence in equation (33) is encapsulated in the factor $\mathcal{F}_{\text{min}}^{(3)}(k)/\mathcal{M}_{\text{min}}(k)$, which applies to PNG with general bispectra. We note that a useful simplification of equation (33) can be made in the $k \lesssim 0.1 \text{ Mpc}^{-1}$ regime of the local template, where $\mathcal{F}_{\text{min}}^{(3)}(k)$ is approximately¹⁰ constant and equal to f_{NL} , and the smoothing kernel, $\bar{W}(k, R)$, in $\mathcal{M}_{\text{min}}(k)$ can be set to unity. In this case, the scale-dependent ionized density bias takes the simplified form¹¹,

$$\Delta b_{\rho_{\text{HII}}}^{(d)}(k, z) = 3f_{\text{NL}} \left[b_{\rho_{\text{HII}}}^{\text{G}}(z) - 1 \right] \frac{\delta_c \Omega_m H_0^2}{g(0)D(z)k^2 \mathcal{T}(k)}, \quad (35)$$

which makes explicit the $1/k^2$ scaling in the limit of $k \ll 1$ for the local template.

3 LINEAR PERTURBATION THEORY OF REIONIZATION (LPTR)

As we have shown in the last section, the ESMR predicts that the large-scale ionized density bias is scale-independent in Gaussian models, and acquires both scale-independent and -dependent corrections in the case with PNG, in a manner analogous to the halo bias. In § 4, we will check these predictions against a more general method, the LPTR of Zhang et al. (2007), which starts with the fundamental equations governing the ionization state of the IGM – the ionization rate and radiative transfer equations. Here we summarize the formalism of Zhang et al. (2007) and our extension of it to include PNG, and in the next section present numerical results from both the ESMR and LPTR.

3.1 Fundamental equations

The main physical quantities which appear in the LPTR formalism are as follows¹²:

¹⁰ The mass thresholds corresponding to $T_{\text{vir}} \sim 10^4 \text{ K}$ are around $M_{\text{min}} = 10^8 M_\odot$. For the corresponding smoothing scales, $\mathcal{F}_{\text{min}}^{(3)}(k)$ deviates from its asymptotic value of f_{NL} by a maximum of a few percent at $k \sim 0.1 \text{ Mpc}^{-1}$.

¹¹ As we discuss in §5 below, the ionized density bias in equations (27), (32), and (35) is *not* equivalent to the “bias of ionized regions” defined by JDFKS, and therefore equation (35) should not be compared directly to their equation (4). In fact, we will show in §5 that equation (35) implies a very different expression for that quantity.

¹² Our notation is different from the original notation of Zhang et al. (2007). See Table 1 for the conversions. These conversions are intended to bring the notation of the LPTR equations

Table 1. LPTR notation conventions

Quantity	Zhang et al. (2007)	This paper
Coordinate vector	\mathbf{x}	\mathbf{r}
Conformal time	τ	η
$\ln \nu - \ln \nu_0$	μ	x_ν
Source emissivity	S	j
Secondary ionization boost factor	κ	$\beta_{\text{S.I.}}$
Mean photon density in units of \bar{n}_{H}	f_γ	$\bar{\xi}_\gamma$
Mean source emissivity in units of \bar{n}_{H}	f_s	$\bar{\xi}_s$
$\ln a$	ω	y
Source spectrum power-law index	β	s

- The total comoving number density of hydrogen atoms (ionized and neutral) and of ionized hydrogen, $n_{\text{H}} = n_{\text{H}}(\mathbf{r}, \eta)$ and $n_{\text{HII}} = n_{\text{HII}}(\mathbf{r}, \eta)$ respectively. Here, \mathbf{r} is the comoving spatial coordinate vector and η is the conformal time.

- $n_\gamma = n_\gamma(\mathbf{r}, \eta, x_\nu, \Omega)$, the comoving number density of photons per unit solid angle, $d^2\Omega$, around the propagation direction Ω , per unit frequency parameter, $x_\nu \equiv \ln \nu - \ln \nu_0$, where ν is the photon frequency, and $\nu_0 = 13.6 \text{ eV} / (2\pi\hbar)$ is the ionization threshold of hydrogen.

- The differential emissivity of the ionizing photon sources: the number of photons emitted per unit comoving volume, per unit conformal time, per unit x_ν , per unit solid angle. Following Zhang et al. (2007), we write the emissivity as $j/4\pi$, where $j = j(\mathbf{r}, \eta, x_\nu, \Omega)$.

The local ionization state of the IGM is governed by the ionization rate equation, a continuity equation which takes into account photoionization and local recombination rates:

$$\frac{\partial n_{\text{HII}}}{\partial \eta} + \nabla \cdot (n_{\text{HII}} \mathbf{u})$$

$$= (n_{\text{H}} - n_{\text{HII}}) \int_0^\infty dx_\nu \int d^2\Omega n_\gamma \frac{\sigma(x_\nu)}{a^2(\eta)} \beta_{\text{S.I.}}(x_\nu, x_i)$$

$$- \frac{\alpha_{\text{B}} n_{\text{HII}}^2}{a^2(\eta)}, \quad (36)$$

where \mathbf{u} is the comoving velocity of a volume-element of ionized hydrogen, $\sigma(x_\nu)$ is the photoionization cross section, $\alpha_{\text{B}} = 2.6 \times 10^{-13} \text{ cm}^3/\text{s}$ is the case-B recombination coefficient at an IGM temperature $T = 10^4 \text{ K}$, and $a(\eta)$ is the cosmological scale factor. In the photoionization term of equation (36), the factor $\beta_{\text{S.I.}}(x_\nu, x_i)$ accounts for secondary ionizations due to energetic free electrons produced when X-ray photons ionize hydrogen. In what follows, we adopt a soft source spectrum which is dominated by UV photons

into closer correspondence with standard notation in the astrophysical literature on radiative transfer and photoionized nebulae.

[see text surrounding equation (41)], such that secondary ionizations are negligible, and $\beta_{\text{S.I.}}$ may be set to unity.

The radiation field that drives the photoionization term in equation (36) evolves according to the radiative transfer equation,

$$\begin{aligned} \frac{\partial n_\gamma}{\partial \eta} + \boldsymbol{\Omega} \cdot \nabla n_\gamma - H(\eta) a(\eta) \frac{\partial n_\gamma}{\partial x_\nu} \\ = \frac{j}{4\pi} - (n_{\text{H}} - n_{\text{HII}}) n_\gamma \frac{\sigma(x_\nu)}{a^2(\eta)}, \end{aligned} \quad (37)$$

where $H(\eta)$ is the Hubble parameter. As in Zhang et al. (2007), we write the main physical quantities in equations (36) and (37) in terms of spatial averages and linear perturbations in the following way:

$$\begin{aligned} n_{\text{HII}} &= \bar{n}_{\text{H}} [\bar{x}_i(\eta) + \Delta_{\text{HII}}(\mathbf{r}, \eta)] \\ n_{\text{H}} &= \bar{n}_{\text{H}} [1 + \delta(\mathbf{r}, \eta)] \\ n_\gamma &= \bar{n}_{\text{H}} [\bar{\xi}_\gamma(\eta, x_\nu) + \Delta_\gamma(\mathbf{r}, \eta, x_\nu, \boldsymbol{\Omega})] \\ j &= \bar{n}_{\text{H}} [\bar{\xi}_s(\eta, x_\nu) + \Delta_s(\mathbf{r}, \eta, x_\nu, \boldsymbol{\Omega})]. \end{aligned} \quad (38)$$

Before going into more detail about the equations governing the spatial averages and linear perturbations, we describe our models of the source emissivity.

3.2 The source emissivity

To facilitate comparison with the analytical expectations derived from the ESMR, we will assume in our LPTR calculations that ACHs provide the only sources of ionizing radiation, so only halos above M_{min} given by equation (13) contribute to the source emissivity.

In what follows, we consider two source models. In the first model, henceforth referred to as “source-model A,” we assume that the number of photons produced in some time interval $\Delta\eta$ is proportional to the change in the number of hydrogen atoms in collapsed halos in that time interval. In this model, photon-production is fueled only by *newly collapsed hydrogen*, which may be a reasonable approximation if either internal or external feedback mechanisms quickly act to limit continuous star formation, and/or if the steep rise in abundance of ACHs results in the effective dominance of reionization by newly collapsed halos. In the second model, “source-model B,” we assume that the *rate* of photon production at a time η is proportional to the number of collapsed hydrogen atoms at that time. In this model, photon-production is continuously fueled by hydrogen once it collapses into halos.

Our motivation for considering the two scenarios above is that source-model A is more similar to the ansatz adopted in the ESMR, where the number of ionizing photons produced in some region is assumed proportional to the number of collapsed baryons in that region. On the other hand, radiative transfer simulations often assume that the photon production rate is proportional to the collapse baryon number, as in source-model B. It is therefore useful to compare results using both assumptions. Physically, these mod-

els represent two limiting cases of source lifetimes. In source-model A the lifetimes are assumed to be much shorter than the duration of reionization, whereas in source-model B they are assumed to be much longer.

Consider the emissivity j smoothed in coordinate space over large scales using a smoothing kernel with characteristic scale R (the Fourier space linear perturbation equations in §3.4 are rendered independent of R in the large-scale limit where $k \ll 2\pi/R$). If we assume that ACHs emit on average $\gamma^A(x_\nu)$ ionizing photons per unit x_ν , per collapsed hydrogen atom, then we may write the smoothed emissivity in source-model A as

$$j_R^A(\mathbf{r}, \eta, x_\nu) = \gamma^A(x_\nu) \frac{\partial}{\partial \eta} [n_{\text{H}}(\mathbf{r}, \eta, R) f_{\text{coll}}(M_{\text{min}}, R, \delta_R, \eta)]. \quad (39)$$

In contrast, the smoothed emissivity in source-model B can be written as

$$j_R^B(\mathbf{r}, \eta, x_\nu) = \gamma^B(x_\nu) n_{\text{H}}(\mathbf{r}, \eta, R) f_{\text{coll}}(M_{\text{min}}, R, \delta_R, \eta), \quad (40)$$

where $\gamma^B(x_\nu)$ is the number of photons emitted per unit x_ν , per unit η , per collapsed hydrogen atom. Following Zhang et al. (2007), we parameterize the source spectrum with a power law in ν ,

$$\gamma^{A,B}(x_\nu) dx_\nu = -\zeta_{\text{LPTR}}^{A,B} (1+s) \exp[(s+1)x_\nu] dx_\nu, \quad (41)$$

where ζ_{LPTR}^A is the total number of photons per collapsed hydrogen atom, per unit x_ν , and ζ_{LPTR}^B is the total number of photons, per unit η , per collapsed hydrogen atom, per unit x_ν . The normalization of equation (41) has been chosen so that $\int_0^\infty \gamma^{A,B}(x_\nu) dx_\nu = \zeta_{\text{LPTR}}^{A,B}$ under the condition $s < -1$. In our numerical results presented in §4, we fix $\zeta_{\text{LPTR}}^{A,B}$ by fixing the value of the electron-scattering optical depth. The power law index, s , can be used to shift the spectrum towards the soft (UV) or hard (X-Ray) photons. In this work, we restrict ourselves to a soft source spectrum, with $s = -3$ [see Zhang et al. (2007) for LPTR calculations with a hard spectrum in models with Gaussian initial conditions].

Finally, we note that the LPTR can be sourced by any model of the collapsed fraction, including those extracted from N-body simulations. However, for the sake of comparison, we use excursion-set equations (14) and (18) in the Gaussian and non-Gaussian models respectively, so the statistics of the halo sources in the ESMR and LPTR calculations are exactly the same. However, we emphasize that the LPTR is otherwise independent of the ESMR in how it models reionization; the former incorporates large-scale physics of radiative transfer, photoionization, and recombinations in the IGM, while the latter follows from the ansatz in equation (12).

3.3 The equations of the spatial averages

The spatial averages of equation (36) and (37) are

$$\begin{aligned} \frac{\partial \bar{x}_i}{\partial \eta} &= 4\pi(1 - \bar{x}_i) \int dx_\nu \frac{\sigma \bar{n}_{\text{H}}}{a^2} \langle \beta_{\text{S.I.}} \rangle \bar{\xi}_\gamma C_{\gamma\text{H}}^{(1)} \\ &\quad - \frac{\alpha_{\text{B}} \bar{n}_{\text{H}}}{a^2} \bar{x}_i^2 C_{\text{HII}} \end{aligned} \quad (42)$$

and

$$\frac{\partial \bar{\xi}_\gamma}{\partial \eta} = \frac{\bar{\xi}_s}{4\pi} + Ha \frac{\partial \bar{\xi}_\gamma}{\partial x_\nu} - \frac{\sigma \bar{n}_H}{a^2} (1 - \bar{x}_i) \bar{\xi}_\gamma C_{\gamma H}^{(2)} \quad (43)$$

respectively, where the quantity $C_{\text{HII}} \equiv \langle n_{\text{HII}}^2 \rangle / \langle n_{\text{HII}} \rangle^2$ is the clumping factor for hydrogen recombination, and

$$C_{\gamma H}^{(1)} \equiv \frac{\langle n_{\text{HI}} n_\gamma \beta_{\text{S.I.}} \rangle}{\langle n_{\text{HI}} \rangle \langle n_\gamma \rangle \langle \beta_{\text{S.I.}} \rangle} \quad (44)$$

and

$$C_{\gamma H}^{(2)} \equiv \frac{\langle n_{\text{HI}} n_\gamma \rangle}{\langle n_{\text{HI}} \rangle \langle n_\gamma \rangle} \quad (45)$$

are the photoionization clumping factors. In the case of a soft source spectrum, in which secondary ionizations are negligible, $C_{\gamma H}^{(1)} \approx C_{\gamma H}^{(2)}$. From here on we will drop the distinction and denote both photoionization factors with $C_{\gamma H}$. These clumping factors cannot be calculated analytically, since they are sensitive to non-linear density fluctuations on small scales, and detailed feedback effects of the radiation background. We therefore employ a few simple models for the clumping factors, motivated by numerical results previously reported in the literature, which we describe in §4.1.

Note that the source emissivity appears in the above spatially averaged equations through the function $\bar{\xi}_s$. In appendix B, we show that $\bar{\xi}_s$ is given by

$$\bar{\xi}_s^A = \gamma^A(x_\nu) \frac{\partial f_{\text{coll},0}}{\partial \eta} \quad (46)$$

in source-model A, and

$$\bar{\xi}_s^B = \gamma^B(x_\nu) f_{\text{coll},0} \quad (47)$$

in source-model B. For Gaussian initial conditions, we insert equation (14) with $\delta_R = 0$ and $S_R = 0$ into the above equations. For non-Gaussian initial conditions, we use (29) along with equation (30).

3.4 The linear perturbation equations

Following Zhang et al. (2007), we substitute the conformal time with the variable $y \equiv \ln a(\eta)$, and define $\hat{\sigma}(\eta, x_\nu) \equiv \sigma(x_\nu) \bar{n}_H / (Ha^3)$ and $\hat{\alpha}_B \equiv \alpha_B \bar{n}_H / (Ha^3)$ for notational convenience. Under these substitutions, $\hat{\sigma}$ represents the probability that a photon propagating through a neutral Universe with frequency parameter x_ν directly ionizes a single atom within a Hubble time. Similarly, $\hat{\alpha}_B$ is the average number of times a proton in a fully ionized universe recombines within a Hubble time. We take the Fourier transforms of equation (36) and (37) and keep only terms that are first-order in the Fourier transforms of δ , Δ_s , Δ_{HII} , and Δ_γ (from here on denoted by $\tilde{\delta}$, $\tilde{\Delta}_s$, $\tilde{\Delta}_{\text{HII}}$, and $\tilde{\Delta}_\gamma$ respectively). Noting that the dark matter density contrast is to first order proportional to the growth factor, $D(\eta)$, and that the peculiar velocity is proportional to the gradient of the gravitational potential, we obtain

$$\frac{\partial \tilde{\Delta}_{\text{HII}}}{\partial y} = F_2 \tilde{\delta} - F_1 \tilde{\Delta}_{\text{HII}} + \int_0^\infty dx_\nu \langle \beta_{\text{S.I.}} \rangle \int d^2 \Omega \tilde{\Delta}_\gamma (1 - \bar{x}_i) \hat{\sigma} \quad (48)$$

and

$$\frac{\partial \tilde{\Delta}_\gamma}{\partial y} = \frac{\partial \tilde{\Delta}_\gamma}{\partial x_\nu} - F_3 \tilde{\Delta}_\gamma + \frac{\tilde{\Delta}_s}{4\pi Ha} + \hat{\sigma} \bar{\xi}_\gamma (\tilde{\Delta}_{\text{HII}} - \tilde{\delta}), \quad (49)$$

where we have defined the following auxiliary functions:

$$F_1 = 2\hat{\alpha}_B \bar{x}_i \quad (50)$$

$$+ 4\pi \int_0^\infty dx_\nu \hat{\sigma} \bar{\xi}_\gamma \left[\langle \beta_{\text{S.I.}} \rangle - (1 - \bar{x}_i) \frac{\partial \beta_{\text{S.I.}}}{\partial \phi} \Big|_{\phi=\bar{x}_i} \right],$$

$$F_2 = \frac{d \ln D}{dy} \bar{x}_i \quad (51)$$

$$+ 4\pi \int_0^\infty dx_\nu \hat{\sigma} \bar{\xi}_\gamma \left[\langle \beta_{\text{S.I.}} \rangle - (1 - \bar{x}_i) \bar{x}_i \frac{\partial \beta_{\text{S.I.}}}{\partial \phi} \Big|_{\phi=\bar{x}_i} \right],$$

$$F_3 = (1 - \bar{x}_i) \hat{\sigma} - \frac{i \mathbf{k} \cdot \boldsymbol{\Omega}}{Ha}, \quad (52)$$

The source emissivity appears in the above equations through the linear source fluctuation, $\tilde{\Delta}_s(k, \eta)$. In appendix B, we show that

$$\tilde{\Delta}_s^A(k, \eta) = \frac{\tilde{\delta}(\mathbf{k}, \eta)}{D(\eta)} \gamma^A(x_\nu) \frac{\partial}{\partial \eta} \{D(\eta) f_{\text{coll},0} [1 + b_{\text{rcoll}}(k, \eta)]\}. \quad (53)$$

in source-model A, and

$$\tilde{\Delta}_s^B(k, \eta) = \tilde{\delta}(\mathbf{k}, \eta) \gamma^B(x_\nu) f_{\text{coll},0} [1 + b_{\text{rcoll}}(k, \eta)] \quad (54)$$

in source-model B, where the collapsed fraction bias, b_{rcoll} , is obtained as described in the last paragraph of appendix B.

The procedure for numerically solving equations (48) and (49) is detailed in Zhang et al. (2007). First, equations (42) and (43) are solved for the global reionization history, which serves as input for the linear perturbation equations. In summary, the linear coordinate transformation in equation (12) of Zhang et al. (2007) is used to change equation (43) into a first-order ordinary differential equation. The resulting equation can be solved for $\bar{\xi}_\gamma$, for some initial \bar{x}_i . The solution for $\bar{\xi}_\gamma$ is then used to find a new solution of equation (42) for \bar{x}_i . This procedure is repeated until $\bar{\xi}_\gamma$ and \bar{x}_i converge, which tends to happen after about ten iterations. A similar procedure is then applied to solve for the linear perturbations. The coordinate transformation in equation (12) of Zhang et al. (2007) is again applied to change equation (49) into a first-order ordinary differential equation. The resulting equation is solved for $\tilde{\Delta}_\gamma$, which is then integrated over $\boldsymbol{\Omega}$ to obtain the monopole perturbation of the radiation field, under the assumption that the monopole of $\tilde{\Delta}_s$ constitutes the main contribution. The monopole perturbation of the radiation field is then used as input for equation (48), and the solutions are iterated until convergence is achieved.

4 RESULTS

4.1 Illustrative models of reionization

Here we describe the five reionization models which are evaluated in this section. The parameters of these models are

Table 2. Illustrative models of reionization

Model	C_{HII}	$C_{\gamma\text{H}}$	Emissivity	Efficiency Parameter ^a
LPTR1	Eq. 55	1	Eq. 39	$\zeta_{\text{LPTR}}^{\text{A}} = 70.3$
LPTR2	2	1	Eq. 39	$\zeta_{\text{LPTR}}^{\text{A}} = 54.2$
LPTR3	10	1	Eq. 39	$\zeta_{\text{LPTR}}^{\text{A}} = 87.5$
LPTR4	Eq. 55	1	Eq. 40	$\zeta_{\text{LPTR}}^{\text{B}} = 11800$
ESMR	N/A	N/A	N/A	$\zeta_{\text{ESMR}} = 50.2$

^a Here, $\zeta_{\text{LPTR}}^{\text{A}}$ gives the number of photons per collapsed hydrogen atom, per unit x_{ν} , while $\zeta_{\text{LPTR}}^{\text{B}}$ gives the number of photons per collapsed hydrogen atom, per H_0^{-1} , per unit x_{ν} .

summarized in Table 2. We consider four models using the LPTR, in which we must specify the recombination and photoionization clumping factors, in addition to the source prescription, i.e. source-model A [eq. (39)] or source-model B [eq. (40)]. In the first model, LPTR1, we use source-model A and C_{HII} varies with redshift according to the fitting formula in Iliev et al. (2007),

$$C_{\text{HII}} = 26.2917 \exp(-0.1822 z + 0.003505 z^2), \quad (55)$$

obtained from a high-resolution, small-scale N-body simulation, which resolved the mass scale of minihalos (for which, e.g., $C_{\text{HII}} = 3.8, 6,$ and 10 at $z = 15, 10,$ and 6 respectively). They computed the clumping factor from the density field of dark matter *outside* of halos; a procedure which assumes as a first-order approximation that the ionized density fluctuations faithfully trace dark matter fluctuations in the IGM. However, the above fit does not account for feedback effects, such as photoionization heating, which act to suppress the clumping by increasing the Jeans scale inside ionized regions.

Most recently, Finlator et al. (2012) confirmed the suppression of the recombination clumping factor by photoionization heating (also see Pawlik et al. 2009; McQuinn et al. 2011; Shull et al. 2012). They found that C_{HII} rises from ~ 1 at $z = 10$ to ~ 3 at $z = 6$. However, they did not resolve the mass scale of minihalos which dominates the small-scale structure responsible for the recombination clumping factor. Nevertheless, as an opposite extreme, we adopt a constant $C_{\text{HII}} = 2$ in LPTR2, which may be more representative of the photo-heated IGM. On the other hand, LPTR3, with $C_{\text{HII}} = 10$, serves as an upper bracket to the range of recombination rates considered in this work. The LPTR4 model is used to illustrate differences between sourcing photons with the differential and cumulative collapsed fraction [see text surrounding equations (39) and (40)]. It has the same clumping factors as LPTR1, but uses source-model B.

The photoionization clumping factor required by these models is more uncertain. Aubert & Teyssier (2010) find from small-scale reionization simulations that $C_{\gamma\text{H}} = 1$ should be a reasonable approximation to the actual value, which they find to be suppressed relative to C_{HII} (also see Kohler et al. 2007). For simplicity, we set $C_{\gamma\text{H}} = 1$ for all of the LPTR models in Table 2. Finally, we also evaluate the ESMR.

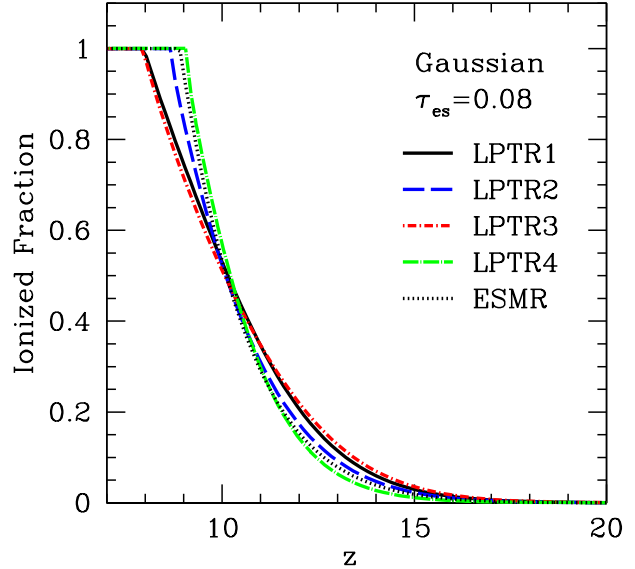


Figure 1. Global reionization histories in models with Gaussian initial conditions (see Table 2 for model parameters). The efficiency parameters in the LPTR models and the ESMR are fixed by setting the electron scattering optical depth to $\tau_{es} = 0.08$.

For a given reionization history, the electron scattering optical depth is

$$\tau_{es} = \sigma_T \int_{z_{\text{rec}}}^0 \bar{n}_e(z) \frac{dt}{dz} dz, \quad (56)$$

where σ_T is the Thompson cross section, $\bar{n}_e(z) = \bar{x}_i(z)\bar{n}_\text{H}(z)$ is the cosmic-average free electron density, and z_{rec} is the redshift of the recombination epoch ($z_{\text{rec}} \approx 10^3$). For all of the above models, we set the normalizations (i.e. by tuning efficiency parameters, either ζ_{LPTR} or ζ_{ESMR}) by fixing $\tau_{es} = 0.08$ in the case with Gaussian initial conditions. When we consider cases with non-zero f_{NL} , the normalization values in the last column of Table 2 stay fixed, while the τ_{es} values vary fractionally by at most a couple of percent for the illustrative $f_{\text{NL}} = \pm 50$ models adopted below, as we show in the next section.

4.2 Global reionization histories

Before presenting our main results for the ionized density bias, it is instructive to consider the global reionization histories in the models of Table 2. A reionization history is obtained in the LPTR by solving for the mean ionized fraction in equations (42) and (43). In Figure 1, we show the mean ionized fraction as a function of redshift for the Gaussian LPTR models of Table 2. We also plot the mean ionized fraction from the ESMR, which is just given by $\bar{x}_i = \zeta_{\text{ESMR}} f_{\text{coll},0}^{\text{G}}$. We note that reionization ends between $z \sim 8-9$ in all of the models shown, which may be at odds with recent observations [see e.g. Robertson et al. (2013) and references therein]. We stress, however, that these mod-

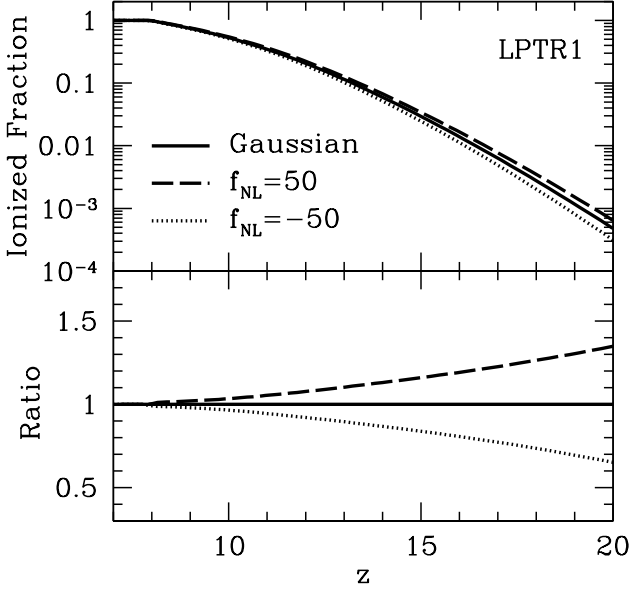


Figure 2. The effects of local PNG on the global reionization history in LPTR1. Note that the source efficiency parameter is fixed to $\zeta_{\text{LPTR}}^{\text{A}} = 70.3$ across all cases shown. Top panel: mean ionized fraction as a function of redshift. Bottom panel: ratio of non-Gaussian to Gaussian models.

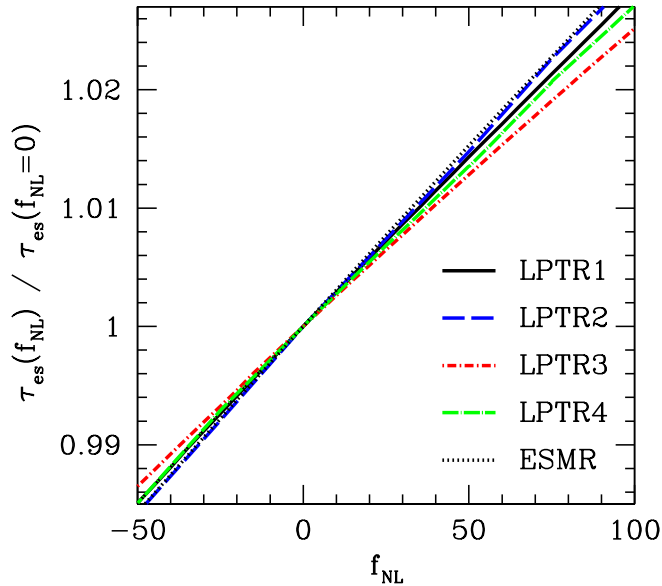


Figure 3. The effects of local PNG on the electron-scattering optical depth, τ_{es} , for a range of f_{NL} values. We show results at a single redshift, $z = 10.2$, corresponding to $\bar{x}_i \approx 50\%$ for all models. Figure 5 shows the redshift evolution of the ionized density bias for a fixed wavenumber, $k = 0.01 \text{ Mpc}^{-1}$. The steep decline of $b_{\rho_{\text{HII}}}$ to unity at lower redshifts marks the end of reionization, after

els are employed below for illustrative purposes to show the effects of PNG on the large-scale structure of reionization.

Figure 2 illustrates how PNG affects the reionization history through its impact on the halo abundance. Although we display only the LPTR1 case for clarity, the results using other models are quantitatively similar. The top panel compares the mean ionized fraction in the Gaussian and non-Gaussian models – the latter with $f_{\text{NL}} = \pm 50$ (we choose these f_{NL} values for illustrative purposes). The normalization of the source emissivity is $\zeta_{\text{LPTR}}^{\text{A}} = 70.3$ in all three cases. The bottom panel shows the ratio of the non-Gaussian to Gaussian \bar{x}_i . The case with $f_{\text{NL}} = 50(-50)$ has an ionized fraction that is $\sim 16\%$ higher(lower) than the Gaussian case at $z \sim 15$, when the universe is only a few percent ionized. However, the differences drop to $\sim 3(1)\%$ when the universe is about 50(95)% ionized at $z \sim 10(8.1)$. Despite the differences early on, all three cases finish reionization at approximately the same redshift, $z \approx 8$. The largest effects of PNG in our models occur at higher redshifts during the early stages of reionization when, due to the imposed M_{min} for ACHs [equation (13)], the collapsed fraction above M_{min} is dominated by halos that are rare at those redshifts. For example, $M_{\text{min}} = 4(5.9)(10) \times 10^7 M_{\odot}$ at $z = 20(15)(10)$, corresponding to a peak height of $\nu \equiv \delta_c / \sqrt{S_{\text{min}}} = 4.5(3.6)(2.6)$.

Since PNG alters the reionization history for a fixed source emissivity, it also alters the optical depth according to equation (56). Figure 3 shows the effects of PNG on τ_{es} for a range of f_{NL} values. For comparison, models with $f_{\text{NL}} \sim 100$ can boost the optical depth by up to only $\sim 3\%$, which is somewhat larger than the results of Crociani et al. (2009). They used an independent analytical model to calculate a $\sim 1\%$ enhancement for local $f_{\text{NL}} \sim 100$.

4.3 Large-scale ionized density bias

Figure 4 shows the ionized density bias as a function of wavenumber for the reionization models in Table 2, with Gaussian (top) and non-Gaussian ($f_{\text{NL}} = 50$, bottom) initial conditions¹³. We show results at a single redshift, $z = 10.2$, corresponding to $\bar{x}_i \approx 50\%$ for all models. Figure 5 shows the redshift evolution of the ionized density bias for a fixed wavenumber, $k = 0.01 \text{ Mpc}^{-1}$. The steep decline of $b_{\rho_{\text{HII}}}$ to unity at lower redshifts marks the end of reionization, after

¹³ The comoving particle horizon is $R \sim 4900 \text{ Mpc}$ at $z \sim 10$, which corresponds to a wavenumber of $k \sim 10^{-3} \text{ Mpc}^{-1}$. While we have adopted the Newtonian approximation in this work, we note that general relativistic effects on the source statistics may come into play on scales approaching $k \sim 10^{-3} \text{ Mpc}^{-1}$ [for detailed studies on galaxy bias in the context of general relativity, see Yoo et al. (2009); Yoo (2010); Bartolo et al. (2011); Challinor & Lewis (2011); Bonvin & Durrer (2011); Baldauf et al. (2011); Bruni et al. (2012); Jeong et al. (2012)]. On the other hand, the mean free path of UV photons during reionization is always much smaller than the horizon, so we do not anticipate additional general relativistic corrections to the LPTR itself to be significant. From a practical viewpoint, such large scales are usually disregarded when forecasting constraints on cosmological parameters from the EoR 21cm power spectrum, because foreground contamination is most problematic on those scales (e.g. Mao et al. 2008). So general relativistic corrections are unlikely to influence the application of our results to the EoR 21cm power spectrum.

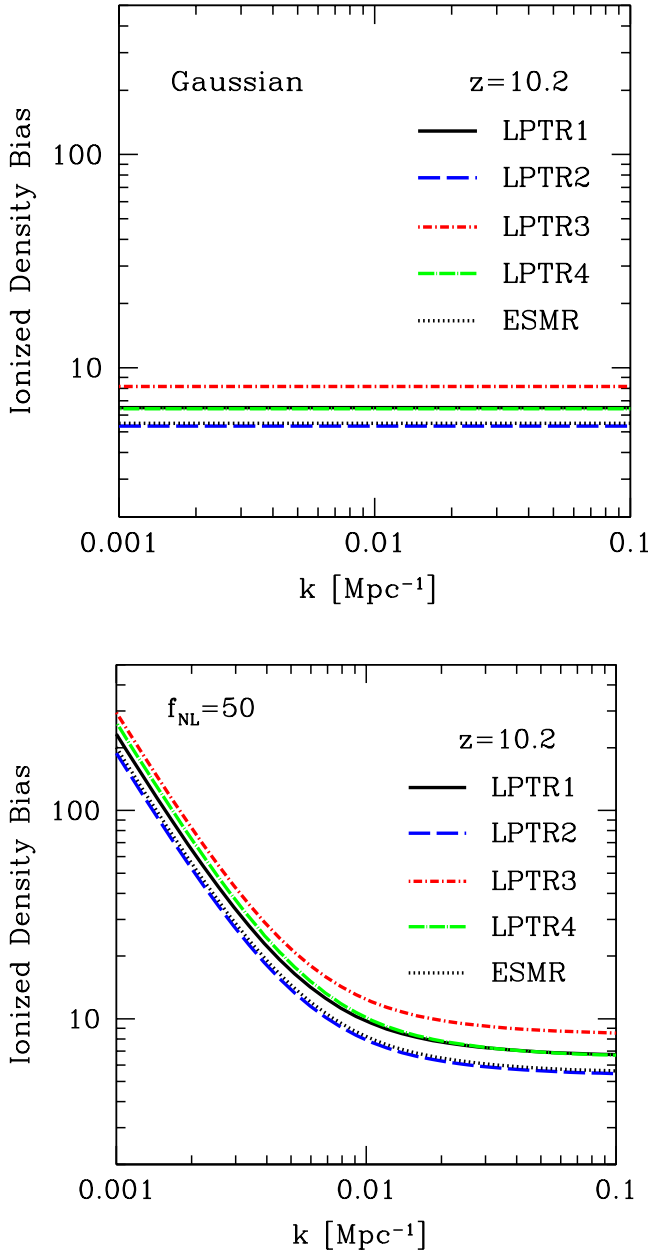


Figure 4. The scale-dependence of the ionized density bias. Top panel: for models with Gaussian initial conditions. Bottom panel: the scale-dependent signature of local PNG with $f_{\text{NL}} = 50$. We show results at a fixed redshift of $z = 10.2$, which corresponds to a global ionized fraction of $\approx 50\%$ in all models shown.

which fluctuations in the IGM ionized density field faithfully trace matter fluctuations (see below for an explanation of the steepness). Figure 6 shows the ionized density bias for a range of f_{NL} values in the LPTR1 model.

Figures 4 and 5 show that the ESMR matches the LPTR2 results particularly well throughout reionization. This is perhaps not surprising, since LPTR2 is the model in Table 2 for which recombinations play the least significant role ($C_{\text{HII}} = 2$). The ESMR also does well at matching the evolution of $b_{\rho_{\text{HII}}}$ in the other LPTR models at early times.

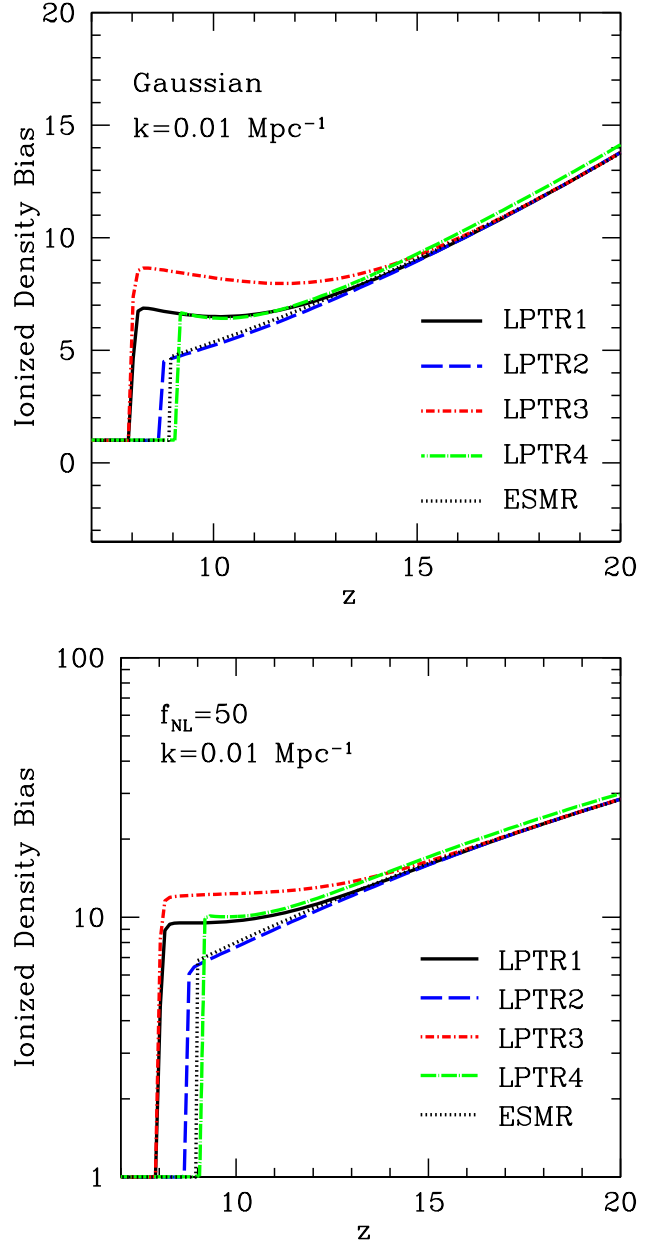


Figure 5. The redshift evolution of the ionized density bias for a fixed scale of $k = 0.01 \text{ Mpc}^{-1}$.

While there are, as one might expect, significant differences in the evolution of $b_{\rho_{\text{HII}}}$ between the ESMR and LPTR models at later times, two basic predictions of the ESMR are corroborated by the LPTR: 1) The Gaussian ionized density bias is scale-independent on large scales. 2) Local PNG introduces through the clustering of sources a strong scale-dependent signature in the ionized density bias.

By construction, the ESMR $b_{\rho_{\text{HII}}}$ is determined by the source bias, so the similarities in shape between the ESMR and LPTR results in Figure 4 confirm, at least at $\bar{x}_i \sim 50\%$, that there is a strong connection between the scale-dependence of the source and ionized density bias parameters. However, we may ask whether this connection is

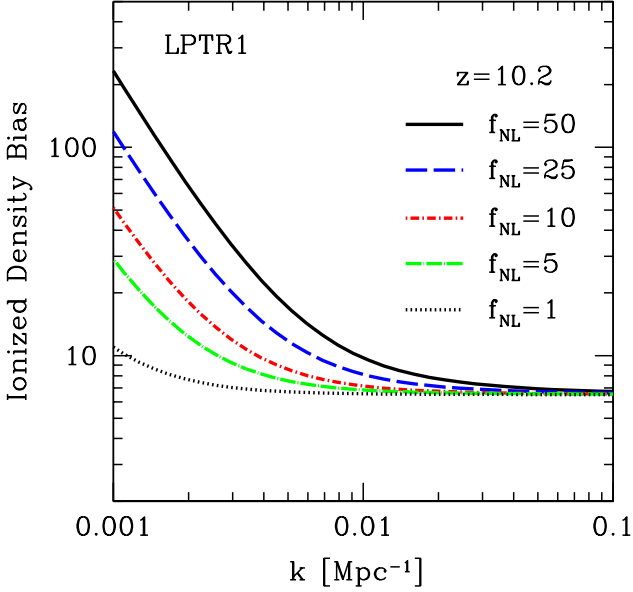


Figure 6. The ionized density bias in LPTR1 at a fixed $z = 10.2$ for a range of local f_{NL} values.

preserved throughout reionization. The answer is not clear a priori, since the LPTR tracks the propagation of ionizing radiation, which can, especially towards the end of reionization, act over long distances to smooth out the patchiness in the ionized density field, and diminish its correspondence with the local clustering of sources. We answer this question by plotting the ionized density bias for a range of scales ($k = 10^{-4}, 10^{-3}, 10^{-2}$ and 0.1 Mpc^{-1}) as a function of redshift. The top and bottom panels of Figure 7 show the Gaussian and non-Gaussian LPTR1 results respectively. Although we focus here on LPTR1 for clarity, we have checked that the results are similar for the other LPTR models in Table 2.

In the top panel of Figure 7, all four curves are so similar that they are indistinguishable in the plot, indicating that the Gaussian $b_{\rho_{\text{HII}}}$ is to a very good approximation scale-independent in the LPTR for $k \lesssim 10^{-1} \text{ Mpc}^{-1}$ effectively throughout all of reionization. In the bottom panel, the different amplitudes of the curves illustrate the scale-dependence of $b_{\rho_{\text{HII}}}$ due to PNG. The important point is that the curves decline at approximately the same rate until the end of reionization, indicating a preservation of their relative amplitudes. This is especially true for the top two curves, corresponding to the largest scales, with $k = 10^{-4}$ and 10^{-3} Mpc^{-1} . The small change with time in the relative amplitude between the bottom two curves, with $k = 10^{-2}$ and 0.1 Mpc^{-1} , results from the scale-independent non-Gaussian correction to the bias, which is only noticeable at larger k , where the scale-dependent term is less dominant.

As Zhang et al. (2007) point out, the preservation of the halo clustering imprint on the ionized density bias can be understood in terms of a characteristic scale – the mean free path of ionizing photons through the IGM – which for a given x_ν is

$$\lambda(x_\nu) = a^2 / [\bar{n}_{\text{H}} \sigma(x_\nu) (1 - \bar{x}_i)]. \quad (57)$$

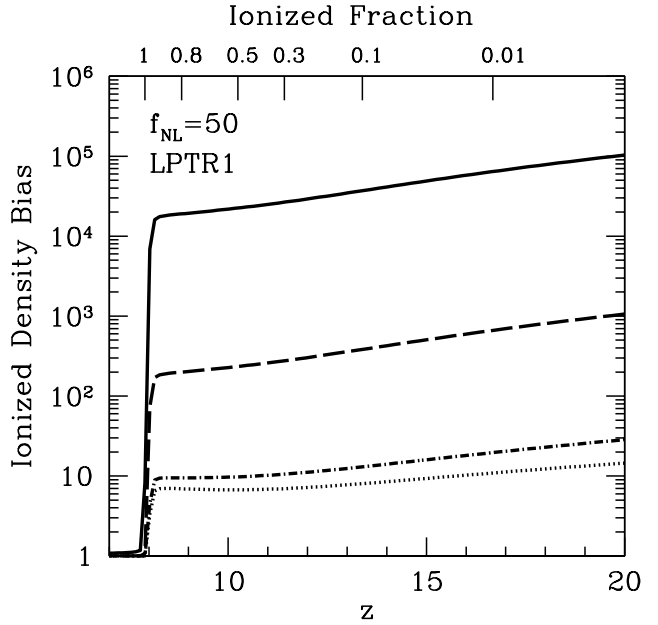
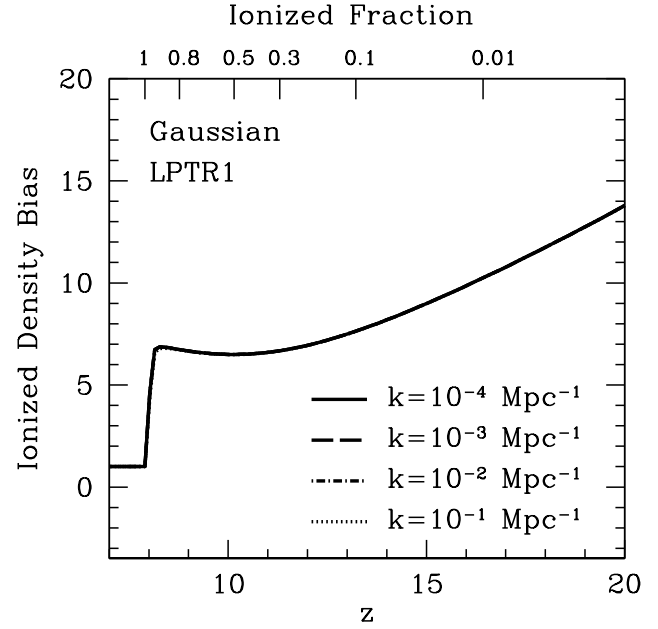


Figure 7. Evolution of the ionized density bias across a range of scales. Top panel: in the LPTR1 model with Gaussian initial conditions. All curves here are degenerate, indicating that the Gaussian ionized density bias remains to a good approximation scale-independent until the end of reionization. Bottom panel: for local PNG with $f_{\text{NL}} = 50$. The line styles here match those in the top panel. The scale-dependent imprint of the non-Gaussian source bias on the ionized density bias is preserved until the end of reionization in the LPTR.

The relevant scale is the ν -averaged mean free path,

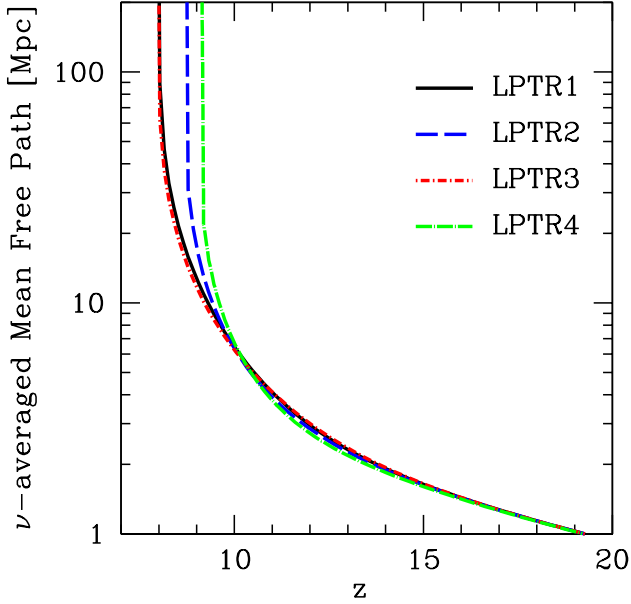


Figure 8. The mean free path of photons through the IGM averaged over frequency ν [see equations (57) and (58)]. The ν -averaged mean free path is the characteristic scale above which fluctuations in the ionized density field correspond to fluctuations in the source distribution. Below this scale, $b_{\rho\text{HII}}$ is suppressed towards unity, since ionized density fluctuations trace matter fluctuations inside of fully ionized regions.

$$\langle \lambda \rangle_\nu = \frac{\int dx_\nu \bar{\xi}_\gamma \lambda(x_\nu)}{\int dx_\nu \bar{\xi}_\gamma}, \quad (58)$$

which corresponds to the average distance that a photon travels before photoionizing a neutral atom. Ionizing radiation is unable to smooth out the patchiness of the ionized density field on scales much larger than $\langle \lambda \rangle_\nu$. On these scales, the ionized density field traces large-scale fluctuations in the sources, so $b_{\rho\text{HII}}$ is expected to have approximately the same scale-dependence as the source bias (though with a different amplitude). On the other hand, for scales less than $\langle \lambda \rangle_\nu$, but larger than the Jeans scale, the ionized density field typically traces the matter density fluctuations, which suppresses the ionized density bias towards $b_{\rho\text{HII}} \sim 1$. As reionization proceeds, $\langle \lambda \rangle_\nu$ increases, so the scale below which $b_{\rho\text{HII}}$ is suppressed increases until $b_{\rho\text{HII}} = 1$ for all scales at the end of reionization.

Figure 8 shows $\langle \lambda \rangle_\nu$ in our four LPTR models. For clarity, we show only the Gaussian models, since the non-Gaussian results are essentially identical. It is now clear why the halo clustering imprint is so well preserved in the LPTR throughout reionization, and why $b_{\rho\text{HII}}$ drops so rapidly to unity at the end of reionization. The value of $\langle \lambda \rangle_\nu$ is well below the scales of interest ($k < 0.1 \text{ Mpc}^{-1}$ corresponding to $\gtrsim 60 \text{ Mpc}$) until the very end of reionization, at which point it is a very steeply rising¹⁴. In fact, $\langle \lambda \rangle_\nu$ increases so

rapidly at the end of reionization that $b_{\rho\text{HII}}$ drops to unity at approximately the same redshift for the four wavenumbers considered in Figure 7. In the next section, we explore the relationship between Gaussian and non-Gaussian $b_{\rho\text{HII}}$ implied by the source-clustering imprint.

4.4 Analytical mapping between Gaussian and non-Gaussian ionized density bias parameters

In the last section we saw the ESMR prediction of a strong scale-dependent imprint in $b_{\rho\text{HII}}$ from the source bias confirmed. On the other hand, the ESMR does not capture the details of the imprint, i.e. the bias amplitude and its evolution, in all of our LPTR models. Indeed, we should not expect it to; after all, the simple ESMR developed in §2 is a one parameter model, whereas each LPTR model contains four parameters (counting the source spectrum slope, s , which we have not varied here). One approach we could take is to expand upon the ESMR by re-parameterizing it to better match the LPTR results. While this may be a fruitful topic of future investigation, it is perhaps more useful at this stage to test whether the ESMR at least gives the correct relationship between the Gaussian and non-Gaussian $b_{\rho\text{HII}}$. To this end, for each LPTR model in Table 2, we consider the accuracy of a “hybrid” calculation, which takes the ESMR equations (32) and (33) for the non-Gaussian $b_{\rho\text{HII}}$, and inserts the numerical values of the Gaussian $b_{\rho\text{HII}}$ from the particular LPTR model. We then compare the results of this calculation to results from the full LPTR calculation.

Figure 9 shows the ratios of $b_{\rho\text{HII}}$ obtained from the hybrid and full LPTR calculations. The top panel shows the ratios as a function of wavenumber for a fixed $z = 10.2$, while the bottom panel shows them as a function of redshift for a fixed $k = 0.01 \text{ Mpc}^{-1}$. Equations (32) and (33) best capture the relationship between Gaussian and non-Gaussian $b_{\rho\text{HII}}$ in the LPTR2 model. In that case, the hybrid result is within 5% of the full result until the end of reionization. Perhaps more importantly, the flatness of the dashed curve in the top panel of Figure 9 shows that the scale-dependence of $b_{\rho\text{HII}}$ is well approximated by the ESMR. For the other LPTR models, the hybrid calculations work best at earlier times, reproducing the LPTR results to within a few percent for $z > 12$ (corresponding to $\bar{x}_i \sim 10\text{--}20\%$) after which the discrepancies tend to rise. Nonetheless, the hybrid calculations are accurate to within $\lesssim 20\%$ across $10^{-3} \lesssim k \lesssim 0.1 \text{ Mpc}^{-1}$ up until the end of reionization for all LPTR models. We highlight the mild mismatch in the scale-dependence of $b_{\rho\text{HII}}$ between the hybrid and full LPTR calculations. This mismatch is most obvious in LPTR3; the model in which recombinations are most significant. In fact, the functional dependence of $b_{\rho\text{HII}}$ on k appears to depend mildly on C_{HII} . This effect may prove to be minimal, if the lower values of C_{HII} ($\sim 1\text{--}3$) suggested by recent studies are confirmed.

Given the success of equations (32) and (33) in mapping to a reasonable accuracy the Gaussian to non-Gaussian $b_{\rho\text{HII}}$ from the range of LPTR models considered here, we hope that these equations will work equally well when applied to more detailed cosmological radiative transfer simulations.

¹⁴ We note that the LPTR neglects absorption of photons by

Lyman-limit systems, which would cap the steep rise of the mean free path at the end of reionization (see Figure 8).

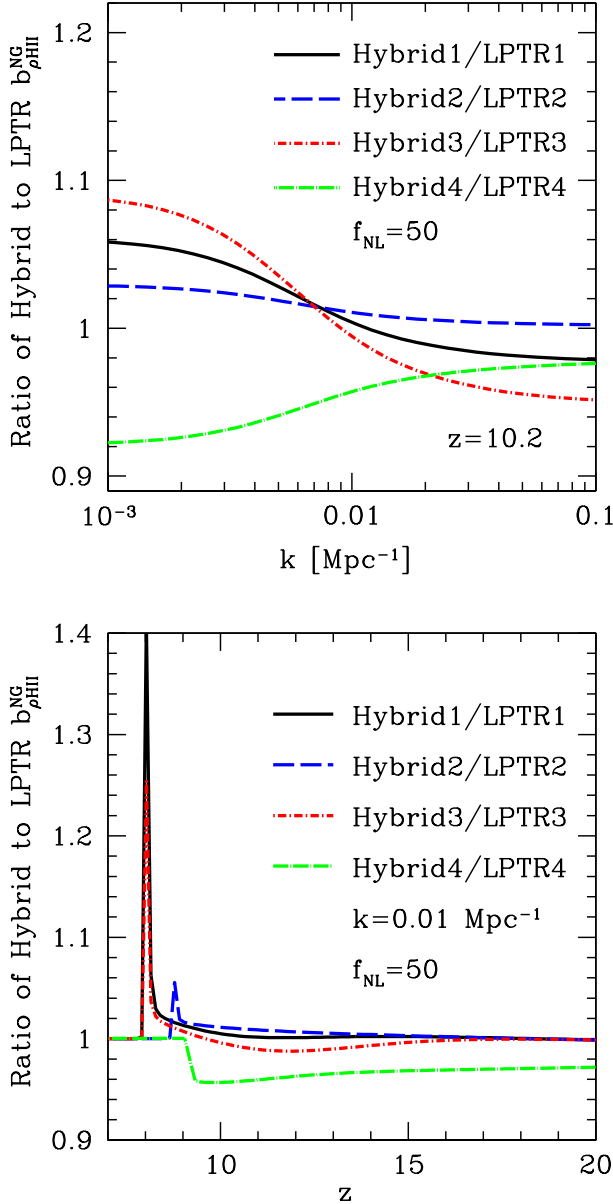


Figure 9. Testing how accurately the ESMR predicts the relationship between Gaussian and non-Gaussian ionized density bias parameters in our LPTR models. In the “hybrid” calculation, for a given LPTR model, we take the Gaussian bias, $b_{\rho_{\text{HII}}}^{\text{G}}$, and insert it into the ESMR expressions [equations (32) and (33)] to obtain the non-Gaussian, $b_{\rho_{\text{HII}}}^{\text{NG}}$. These results are then compared to the full LPTR calculation, which provides the exact $b_{\rho_{\text{HII}}}^{\text{NG}}$. Above, we show the ratio of hybrid to full LPTR $b_{\rho_{\text{HII}}}^{\text{NG}}$ as a function of k for fixed $z = 10.2$ (top), and as a function of z for fixed $k = 0.01 \text{ Mpc}^{-1}$ (bottom).

Equations (32) and (33) should be similarly tested against full simulation results once large enough boxes become available.

5 COMPARISON WITH PREVIOUS WORK

In this section we compare our results to the results of JD-FKS. We begin by summarizing important details of the JD-FKS SimFast21 reionization simulations [see Santos et al. (2010) for details on the SimFast21 code methodology]. Their initial density fields, both Gaussian and non-Gaussian, were generated on a regular cubic mesh with $N = 2048^3$ cells in a $(3 \text{ Gpc})^3$ volume, corresponding to a halo mass-resolution of $M \approx 5 \times 10^{11} M_{\odot}$. In order to account for mass in smaller halos, down to their ACH mass-threshold of $M_{\text{min}} = 10^8 M_{\odot}$, JDFKS employed an analytical sub-grid model in which equation (14) – the excursion-set expression for the *Gaussian* collapsed fraction – is used to fill in the unresolved collapsed mass in each mesh cell (Joudaki et al. 2011). At $z = 7.5$, the redshift at which their analysis was based, the $10^8 M_{\odot}$ threshold corresponds to a peak height of $\nu \equiv \delta_c / \sqrt{S} \approx 2$, while the $5 \times 10^{11} M_{\odot}$ mass-resolution limit corresponds to $\nu \approx 4.7$. Their reionization simulations were therefore sourced mainly by unresolved sub-grid halos, since these were by far more abundant than halos resolved directly by their mesh.

As we point out in § 1, JDFKS did not directly calculate the ionized density bias. Rather, they calculated a quantity they called the “bias of ionized regions,” whose definition has caused some confusion in the literature. They defined this bias parameter to be $\hat{b}_x \equiv \sqrt{\mathcal{P}_{xx} / \mathcal{P}_{\delta\delta}}$ (Note that we use the “hat” notation to distinguish this quantity from the distinct but related ionized fraction bias, b_x . See below for the relationship between \hat{b}_x and b_x). Here, $\mathcal{P}_{\delta\delta} \equiv \hat{T}_b^2 \bar{x}_H^2 P_{\delta\delta}$ and $\mathcal{P}_{xx} \equiv \hat{T}_b^2 P_{xx}$, where \hat{T}_b is related to the spatially averaged 21cm brightness temperature (\bar{T}_b) by $\hat{T}_b = \bar{T}_b / \bar{x}_H$ under the usual assumption that the spin temperature is much greater than the CMB temperature, as expected during reionization. We emphasize the important distinction between \hat{b}_x , used in JDFKS, and the ionized fraction bias, b_x , defined in equation (8). These quantities are related as follows: $\hat{b}_x = \sqrt{\mathcal{P}_{xx} / \mathcal{P}_{\delta\delta}} = (1 / \bar{x}_H) \sqrt{P_{xx} / P_{\delta\delta}} = (\bar{x}_i / \bar{x}_H) \sqrt{P_{\delta_x \delta_x} / P_{\delta\delta}}$, which yields

$$\hat{b}_x = \frac{\bar{x}_i}{\bar{x}_H} b_x. \quad (59)$$

Using equation (9), we also find a simple relationship between \hat{b}_x and the ionized density bias, $b_{\rho_{\text{HII}}}$, which applies on large scales:

$$\hat{b}_x(k, z) = \frac{\bar{x}_i(z)}{\bar{x}_H(z)} [b_{\rho_{\text{HII}}}(k, z) - 1]. \quad (60)$$

JDFKS report that the \hat{b}_x computed from their non-Gaussian simulations are to a good approximation related to the \hat{b}_x from corresponding Gaussian simulations by the following proposed fitting function¹⁵:

¹⁵ Here we restore a factor of $g(0)$ in the denominator of the scale-dependent term. JDFKS did not normalize $D(0) = 1$, so $g(0)$ does not appear in equation (4) of their paper; it is absorbed into their definition of $D(z)$ (Joudaki 2013). In contrast, we choose to normalize $D(0) = 1$, so $g(0)$ must appear in the denominator of our equation (61).

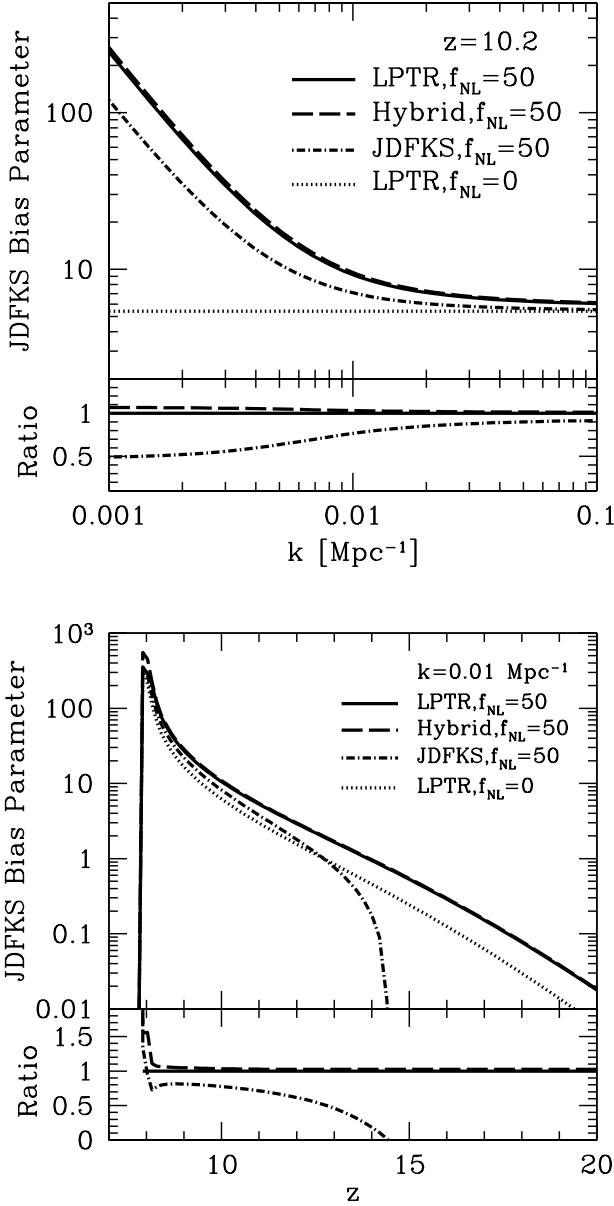


Figure 10. Testing the accuracy of our ESMR prediction [eq. (63)] versus the JDFKS fitting formula [eq. (61)] in predicting the relationship between Gaussian and non-Gaussian $\hat{b}_x = \sqrt{\mathcal{P}_{xx}/\mathcal{P}_{\delta\delta}}$ (The JDFKS bias parameter) in our LPTR calculations. To obtain the curve labeled “hybrid”, we take \hat{b}_x^G from LPTR1 and insert it into equation (63). The curve labeled “JDFKS” is obtained in a similar way, but using (61). For clarity, we only show results from the LPTR1 model in Table 2.

$$\hat{b}_x^{\text{NG}}(k, z) = \hat{b}_x^{\text{G}}(z) + 3f_{\text{NL}} \left[\hat{b}_x^{\text{G}}(z) - 1 \right] \frac{\bar{\delta}_x \Omega_m H_0^2}{g(0)D(z)k^2\mathcal{T}(k)}. \quad (61)$$

The quantity $\bar{\delta}_x$ is analogous to the critical overdensity for collapse which appears in the well-known non-Gaussian halo bias formula (Matarrese & Verde 2008; Dalal et al. 2008; Afshordi & Tolley 2008). The condition $f_{\text{coll}}(M_{\text{min}}, R, z) \geq$

ζ_{ESMR}^{-1} for a fully ionized region in the ESMR along with equation (14) implies (for Gaussian initial conditions) a minimum linearly extrapolated overdensity of

$$\delta_x \geq \delta_c - \sqrt{2}K(\zeta_{\text{ESMR}})\sqrt{S_{\text{min}} - S_R} \quad (62)$$

for a region with Lagrangian radius R to self-ionize, where $K(\zeta_{\text{ESMR}}) \equiv \text{erf}^{-1}(1 - \zeta_{\text{ESMR}}^{-1})$. JDFKS defined $\bar{\delta}_x$ to be the “average” δ_x . For illustrative purposes, they calculated $\bar{\delta}_x = 1.1$ by averaging equation (62) over the fraction of volume filled by H II bubbles. However, they set $\bar{\delta}_x = 1$ for convenience when they used equation (61) to forecast 21cm power spectrum constraints on f_{NL} .

We note that equation (61) was not derived from analytical theory. Rather, it was postulated by JDFKS based on their intuition from previous literature on the halo bias. Here, we derive a formula for \hat{b}_x^{NG} from first principles in the ESMR, and compare it directly to equation (61). We then compare the accuracies of our result and equation (61) in capturing the relationship between \hat{b}_x^{NG} and \hat{b}_x^{G} when both quantities are computed numerically with the LPTR.

To derive our analogue of the JDFKS fitting formula from the ESMR, we use equation (60) to convert equation (27) to \hat{b}_x^{NG} . Note that PNG alters the mean ionized fraction relative to the Gaussian case at a fixed redshift. We will therefore use the super-scripts “NG” and “G” on the mean ionized and neutral fractions to distinguish the two cases. Taking this caveat into account, equation (27) implies

$$\hat{b}_x^{\text{NG}} = \frac{\bar{x}_i^{\text{NG}} \bar{x}_H^{\text{G}}}{\bar{x}_H^{\text{NG}} \bar{x}_i^{\text{G}}} \left\{ \hat{b}_x^{\text{G}} - \frac{\mathcal{S}_{\text{min}}^{(3)}}{6} S_{\text{min}} \hat{b}_x^{\text{G}} \left[\frac{3\delta_c S_{\text{min}} - \delta_c^3}{S_{\text{min}}^2} \right] + \left(\frac{\bar{x}_H^{\text{G}} \hat{b}_x^{\text{G}}}{\bar{x}_i^{\text{G}}} \right) \left(\frac{\delta_c^2}{S_{\text{min}}} - 1 \right) \right\} + 2\delta_c \hat{b}_x^{\text{G}} \frac{\mathcal{F}_{\text{min}}^{(3)}(k)}{\mathcal{M}_{\text{min}}(k)}. \quad (63)$$

Note that this expression applies to PNG with general bispectra. In order to compare this result to the JDFKS formula [equation (61)] we restrict equation (63) to the local template, where we can make the substitution,

$$2\delta_c \hat{b}_x^{\text{G}} \frac{\mathcal{F}_{\text{min}}^{(3)}(k)}{\mathcal{M}_{\text{min}}(k)} \rightarrow 3f_{\text{NL}} \hat{b}_x^{\text{G}} \delta_c \frac{\Omega_m H_0^2}{g(0)D(z)k^2\mathcal{T}(k)}. \quad (64)$$

Applying this substitution to equation (63) yields

$$\hat{b}_x^{\text{NG}} = \frac{\bar{x}_i^{\text{NG}} \bar{x}_H^{\text{G}}}{\bar{x}_H^{\text{NG}} \bar{x}_i^{\text{G}}} \left\{ \hat{b}_x^{\text{G}} - \frac{\mathcal{S}_{\text{min}}^{(3)}}{6} S_{\text{min}} \hat{b}_x^{\text{G}} \left[\frac{3\delta_c S_{\text{min}} - \delta_c^3}{S_{\text{min}}^2} \right] + \left(\frac{\bar{x}_H^{\text{G}} \hat{b}_x^{\text{G}}}{\bar{x}_i^{\text{G}}} \right) \left(\frac{\delta_c^2}{S_{\text{min}}} - 1 \right) \right\} + 3f_{\text{NL}} \hat{b}_x^{\text{G}} \frac{\delta_c \Omega_m H_0^2}{g(0)D(z)k^2\mathcal{T}(k)}. \quad (65)$$

Our analytical result differs from the JDFKS fitting formula in several important ways: (i) The second term in equation (65) is the scale-independent correction to \hat{b}_x due to PNG, which JDFKS neglected. For the local template, this correction contributes up to a few percent to \hat{b}_x for $k \sim 0.1 \text{ Mpc}^{-1}$. As an example, in the ESMR model at $z = 10.2$ with $f_{\text{NL}} = 50$ ($\bar{x}_i^{\text{NG}} = 0.51$, $\bar{x}_i^{\text{G}} = 0.48$, $\hat{b}_x^{\text{G}} = 4.15$), we find the fractional contribution of the scale-independent term to be 2.5, 1.6 and 0.06 percent at $k = 10^{-1}$, 10^{-2} , and 10^{-3} Mpc^{-1} respectively. (ii) The critical density for

halo collapse, $\delta_c \approx 1.686$, appears in the last term of (63) (the scale-dependent term) and not $\bar{\delta}_x \approx 1$ as assumed by JDFKS. (iii) Equation (63) has an overall factor involving mean ionized and neutral fractions which is absent in the JDFKS formula. (iv) It is \hat{b}_x^G that sets the amplitude of the scale-dependent term in our formula, and not $(b_x^G - 1)$ as assumed by JDFKS. They assumed the latter because the non-Gaussian scale-dependent Eulerian halo bias is proportional to $(b^G - 1)$, where b^G is the Gaussian (Eulerian) halo bias. This $(b^G - 1)$ form in the halo bias comes from the spherical collapse model, in which the Lagrangian and Eulerian halo bias parameters are related by $b^G = b_L^G + 1$ (Mo & White 1996). However, as we discussed in §2.3.1, the Lagrangian and Eulerian ionized fraction bias parameters are equivalent, and since $\hat{b}_x = (\bar{x}_i/\bar{x}_H)b_x$, so are the Lagrangian and Eulerian \hat{b}_x . The factor of $(\hat{b}_x^G - 1)$ should therefore not appear in the formula.

We now explore the numerical differences between equations (61) and (63). Figure 10 shows the comparison between three calculations: (i) The purely numerical LPTR1 calculation (solid), using equation (60) to convert $b_{\rho_{\text{HII}}}^{\text{NG}}$ to \hat{b}_x^{NG} , (ii) Our ESMR prediction (dashed), equation (63), and (iii) The JDFKS fitting formula (dot-dashed), equation (61). In calculations ii and iii, we insert the numerical values of \hat{b}_x^G from the LPTR1 calculation into equations (63) and (61) respectively (like the “hybrid” calculations described in the last section), since our goal here is to determine how well these equations capture the mapping between \hat{b}_x^G and \hat{b}_x^{NG} . The top panel shows \hat{b}_x as a function of k at a fixed redshift of $z = 10.2$, corresponding to a mean ionized fraction of $\approx 50\%$. The bottom panel shows the redshift evolution for a fixed $k = 0.01 \text{ Mpc}^{-1}$. While the ESMR prediction matches the LPTR results well, the JDFKS fitting function always yields a significantly lower amplitude of \hat{b}_x^{NG} . The differences can be quantified in terms of f_{NL} , which sets the amplitude of the scale-dependent term. As a simple, “back-of-the-envelope” illustration, if we assume that $f_{\text{NL}} = 50$ is the “true” model, and that the LPTR1 curve in the top panel of Figure 10 represents the “measured” \hat{b}_x^{NG} at $\bar{x}_i \sim 0.5$, then an observer using the JDFKS fitting formula would falsely infer an $f_{\text{NL}} \sim 100$, assuming that \hat{b}_x^G is known exactly. The bottom panel of Figure 10 shows that the JDFKS formula also does not reproduce the redshift evolution of \hat{b}_x^{NG} . At high redshifts, the JDFKS formula becomes negative due to \hat{b}_x^G dropping below unity at those epochs. This behavior of the JDFKS fitting formula is not observed in our results.

6 SUMMARY AND DISCUSSION

We have presented a first-principals investigation on the effects of primordial non-Gaussianity on the large-scale structure of reionization. We employed two methods that are independent in how they model reionization: 1) An extension of the analytical excursion-set model of reionization (ESMR) of Furlanetto et al. (2004) to include PNG, which allowed us to derive analytical expressions for the ionized density bias. 2) The linear perturbation theory of reionization (LPTR) of Zhang et al. (2007), which has the advantage that it directly solves the ionization rate and radiative transfer equations, allowing us to explore a range of recombination clumping

factors, and two distinct models of photon-production rates in galactic sources. Our main results can be summarized as follows:

- Equations (18) and (19) inserted into equation (12) constitute our extension of the analytical ESMR of Furlanetto et al. (2004) to include non-Gaussian initial conditions with general bispectra.

- In our non-Gaussian extension of the ESMR, equation (26) gives the Gaussian ionized density bias, while equations (32) and (33) give the non-Gaussian scale-independent and -dependent ionized density bias corrections. These expressions follow from the assumption that, on large scales, fluctuations in the ionized density field follow fluctuations in the source distribution. The ESMR predicts that the ionized density bias is scale-independent in models with Gaussian initial conditions, while for non-Gaussian initial conditions the bias acquires a scale-dependent correction which scales as $1/k^2$ in the local template for small k .

- Numerical calculations using the LPTR confirm that the ionized density bias in the small- k limit ($k < 0.1 \text{ Mpc}^{-1}$) is scale-independent in models with Gaussian initial conditions, and strongly scale-dependent for local PNG, reflecting the impact of PNG on the source bias. Moreover, the imprint of the source bias on the ionized density bias persists throughout the reionization epoch. We attribute this characteristic of our models to the mean free path of UV photons through the IGM, which remains small relative to the scales on which PNG affects the halo bias, until just before reionization ends.

- While the simple one-parameter ESMR model developed in this work cannot capture the detailed evolution of even the Gaussian ionized density bias computed in the LPTR, we found that equations (32) and (33) provide a reasonably accurate map between Gaussian and non-Gaussian ionized density bias parameters. As shown in Figure 9, these formulae work best at earlier times, corresponding to lower mean ionized fractions, and in models with lower recombination rates.

- Equation (63) gives our prediction for the “bias of ionized” regions defined by JDFKS, which is related to the ionized density bias used in this work by equation (60). This result can be compared directly to the JDFKS fitting formula given in equation (61), which they used to forecast constraints on f_{NL} by future measurements of the EoR 21cm power spectrum. We note significant differences in the forms of these expressions. In a companion paper, we use our result to revisit the topic of constraining PNG with the EoR 21cm power spectrum (Mao et al. 2013).

There are several scenarios one could imagine which might require extensions to both our analytical ESMR predictions and our LPTR calculations. For example, all of our models assumed that atomic cooling halos were the only photon-sources during reionization. These were not the first halos to form stars, however, and there was likely a modest contribution to reionization from minihalos at earlier times before feedback mechanisms effectively shut them down (see e.g. Ahn et al. 2012). We also did not take into account the possible “self-regulation” effects of reionization on the star formation rates of lower mass atomic cooling halos, below the Jeans filtering scale, $M \sim 10^9 M_\odot$. These feedback effects can lead to a more complicated reionization

history and possibly a more complicated evolution and scale dependence of the ionized density bias (for studies on the role of feedback during reionization, see e.g. Shapiro et al. 1994; Chiu & Ostriker 2000; Haiman & Holder 2003; Wyithe & Loeb 2003; Onken & Miralda-Escudé 2004; Furlanetto & Loeb 2005; Kramer et al. 2006; Iliev et al. 2007; Wyithe & Morales 2007; Wyithe & Cen 2007; Mesinger & Dijkstra 2008; Kulkarni & Choudhury 2011; Alvarez & Abel 2012; Ahn et al. 2012; Sobacchi & Mesinger 2013).

We have also assumed in the case with no feedback that the bias of ionizing sources is equal to the halo bias. This assumption is often adopted in the literature, but its accuracy is uncertain. One situation in which this assumption might not hold is if mergers play a significant role in driving star formation during reionization (see e.g. Lemastra et al. (2013) for recent observations at lower redshifts). In this case, the source bias might be quite different from the halo bias, since the bias of merging halos is different from the general halo population. This difference would likely be reflected in the ionized density bias, and it is not clear whether our current ESMR expressions would apply in such a scenario [see Cohn & Chang (2007) for an extension of the Gaussian ESMR to include the effects of halo mergers]. Scenarios in which the source bias is not simply related to the halo bias should be explored to gauge their impact on the ionized density bias.

We have considered a range of reionization models in this work, but there is an important characteristic in common with all of these models. The mean free path of typical photons through the IGM is short relative to the large scales of interest, until the end of reionization. This characteristic is a consequence of the soft source spectrum we adopted. As noted above, this feature is crucial in preserving the imprint of the source bias on the large-scale ionized density bias. It is therefore important to consider scenarios in which this condition might not hold. One such scenario is that of a hard source spectrum, i.e. a significant contribution from X-ray photons, which have a significantly larger mean free path relative to UV photons, and may therefore act to suppress the amplitude of the ionized density bias on larger scales, approaching the scales of interest for the effects of PNG. Further numerical work should be devoted towards exploring more detailed reionization models and their implications for the analytical results presented here.

Finally, we have discussed one observable effect of the scale-dependent ionized density bias: a scale-dependent signature in the EoR 21cm power spectrum. However, the scale-dependent ionized density bias can also have an impact on secondary temperature and polarization anisotropies in the CMB sourced by the EoR. Extensions of this work may also involve observational signatures beyond the redshifted 21cm background.

Note: during the preparation of this manuscript, a paper appeared on the ArXiv preprint archive on the topic of constraining PNG with the EoR 21cm power spectrum (Chongchitnan 2013). Chongchitnan (2013) calculated the ionized fraction bias (and not the ionized density bias considered in our work) based on the reionization model of Alvarez et al. (2006). We note that the approach of Chongchitnan (2013) does not yield an analytical expression for the non-Gaussian ionized fraction bias, in con-

trast to the ESMR approach taken here. Shortly after this manuscript was submitted, a paper by Lidz et al. (2013) appeared on the archive which expanded upon the work of JDFKS with more-detailed semi-numerical simulations of reionization with PNG. They also considered the effects of foreground subtraction in their forecasts of constraints on f_{NL} from the EoR 21cm power spectrum.

ACKNOWLEDGMENTS

A.D. thanks Vincent Desjacques, Donghui Jeong, and Ei-ichiro Komatsu for useful discussions, and Steve Furlanetto for helpful comments on this manuscript. The authors also thank Shahab Joudaki and Mario Santos for additional information on the work in JDFKS, and the referee of this manuscript for helpful comments. This work was supported in part by U.S. NSF grants AST-0708176 and AST-1009799, and NASA grants NNX07AH09G and NNX11AE09G. YM was supported by the French state funds managed by the ANR within the Investissements d’Avenir programme under reference ANR-11-IDEX-0004-02.

REFERENCES

- Acquaviva V., Bartolo N., Matarrese S., Riotto A., 2003, Nuclear Physics B, 667, 119
- Ade P. A. R., Aghanim N., Armitage-Caplan C., Arnaud M., Ashdown M., Atrio-Barandela F., Aumont J., Baccigalupi C., Banday A. J., et al. 2013, ArXiv e-prints
- Adshard P., Baxter E. J., Dodelson S., Lidz A., 2012, PRD, 86, 063526
- Afshordi N., Tolley A. J., 2008, PRD, 78, 123507
- Agullo I., Parker L., 2011, PRD, 83, 063526
- Agullo I., Shandera S., 2012, JCAP, 9, 7
- Ahn K., Iliev I. T., Shapiro P. R., Mellema G., Koda J., Mao Y., 2012, ApJ, 756, L16
- Alvarez M. A., Abel T., 2012, ApJ, 747, 126
- Alvarez M. A., Komatsu E., Doré O., Shapiro P. R., 2006, ApJ, 647, 840
- Aubert D., Teyssier R., 2010, ApJ, 724, 244
- Babich D., Creminelli P., Zaldarriaga M., 2004, JCAP, 8, 9
- Babich D., Zaldarriaga M., 2004, PRD, 70, 083005
- Baldauf T., Seljak U., Senatore L., Zaldarriaga M., 2011, JCAP, 10, 31
- Barkana R., Loeb A., 2005, ApJ, 624, L65
- Bartolo N., Matarrese S., Riotto A., 2011, JCAP, 4, 11
- Bennett C. L., Larson D., Weiland J. L., Jarosik N., Hinshaw G., Odegard N., Smith K. M., Hill R. S., et al. 2012, ArXiv e-prints
- Bond J. R., Cole S., Efstathiou G., Kaiser N., 1991, ApJ, 379, 440
- Bonvin C., Durrer R., 2011, PRD, 84, 063505
- Bruni M., Crittenden R., Koyama K., Maartens R., Pitrou C., Wands D., 2012, PRD, 85, 041301
- Carney D., Fischler W., Paban S., Sivanandam N., 2012, JCAP, 12, 12
- Challinor A., Lewis A., 2011, PRD, 84, 043516
- Chen X., Firouzjahi H., Namjoo M. H., Sasaki M., 2013, ArXiv e-prints

- Chen X., Huang M.-x., Kachru S., Shiu G., 2007, *JCAP*, 1, 2
- Cheung C., Fitzpatrick A. L., Kaplan J., Senatore L., 2008, *JCAP*, 2, 21
- Chiu W. A., Ostriker J. P., 2000, *ApJ*, 534, 507
- Chongchitnan S., 2013, ArXiv e-prints
- Chongchitnan S., Silk J., 2012, *MNRAS*, 426, L21
- Cohn J. D., Chang T.-C., 2007, *MNRAS*, 374, 72
- Cooray A., Sheth R., 2002, *Physics Reports*, 372, 1
- Creminelli P., Zaldarriaga M., 2004, *JCAP*, 10, 6
- Crociani D., Moscardini L., Viel M., Matarrese S., 2009, *MNRAS*, 394, 133
- Dalal N., Doré O., Huterer D., Shirokov A., 2008, *PRD*, 77, 123514
- D'Aloisio A., Zhang J., Jeong D., Shapiro P. R., 2012, ArXiv e-prints
- D'Amico G., Musso M., Noreña J., Paranjape A., 2011, *PRD*, 83, 023521
- Desjacques V., Jeong D., Schmidt F., 2011a, *PRD*, 84, 061301
- Desjacques V., Jeong D., Schmidt F., 2011b, *PRD*, 84, 063512
- Desjacques V., Seljak U., 2010a, *Classical and Quantum Gravity*, 27, 124011
- Desjacques V., Seljak U., 2010b, *PRD*, 81, 023006
- Dey A., Kovetz E., Paban S., 2012, *JCAP*, 10, 55
- Dey A., Paban S., 2012, *JCAP*, 4, 39
- Eisenstein D. J., Hu W., 1999, *ApJ*, 511, 5
- Finlator K., Oh S. P., Özel F., Davé R., 2012, ArXiv e-prints
- Furlanetto S. R., Loeb A., 2005, *ApJ*, 634, 1
- Furlanetto S. R., Oh S. P., Briggs F. H., 2006, *Physics Reports*, 433, 181
- Furlanetto S. R., Zaldarriaga M., Hernquist L., 2004, *ApJ*, 613, 1
- Ganc J., 2011, *PRD*, 84, 063514
- Ganc J., Komatsu E., 2012, *PRD*, 86, 023518
- Gangui A., Lucchin F., Matarrese S., Mollerach S., 1994, *ApJ*, 430, 447
- Giannantonio T., Ross A. J., Percival W. J., Crittenden R., Bacher D., Kilbinger M., Nichol R., Weller J., 2013, ArXiv e-prints
- Grossi M., Dolag K., Branchini E., Matarrese S., Moscardini L., 2007, *MNRAS*, 382, 1261
- Grossi M., Verde L., Carbone C., Dolag K., Branchini E., Iannuzzi F., Matarrese S., Moscardini L., 2009, *MNRAS*, 398, 321
- Haiman Z., Abel T., Rees M. J., 2000, *ApJ*, 534, 11
- Haiman Z., Holder G. P., 2003, *ApJ*, 595, 1
- Hodges H. M., Blumenthal G. R., Kofman L. A., Primack J. R., 1990, *Nuclear Physics B*, 335, 197
- Iliev I. T., Mellema G., Shapiro P. R., Pen U.-L., 2007, *MNRAS*, 376, 534
- Jeong D., Schmidt F., Hirata C. M., 2012, *PRD*, 85, 023504
- Joudaki S., 2013, private communication
- Joudaki S., Doré O., Ferramacho L., Kaplinghat M., Santos M. G., 2011, *Physical Review Letters*, 107, 131304
- Kamionkowski M., Verde L., Jimenez R., 2009, *JCAP*, 1, 10
- Kofman L., Blumenthal G. R., Hodges H., Primack J. R., 1991, in Latham D. W., da Costa L. A. N., eds, *Large-scale Structures and Peculiar Motions in the Universe* Vol. 15 of *Astronomical Society of the Pacific Conference Series*, Generation of Non-Flat and Non-Gaussian Perturbations from Inflation. p. 339
- Kohler K., Gnedin N. Y., Hamilton A. J. S., 2007, *ApJ*, 657, 15
- Komatsu E., Smith K. M., Dunkley J., Bennett C. L., Gold B., Hinshaw G., Jarosik N., Larson D., et al. 2011, *ApJS*, 192, 18
- Komatsu E., Spergel D. N., 2001, *PRD*, 63, 063002
- Kramer R. H., Haiman Z., Oh S. P., 2006, *ApJ*, 649, 570
- Kulkarni G., Choudhury T. R., 2011, *MNRAS*, 412, 2781
- Lacey C., Cole S., 1993, *MNRAS*, 262, 627
- Lamastra A., Menci N., Fiore F., Santini P., 2013, ArXiv e-prints
- Lidz A., Baxter E. J., Adshead P., Dodelson S., 2013, ArXiv e-prints
- Lo Verde M., Miller A., Shandera S., Verde L., 2008, *Journal of Cosmology and Astro-Particle Physics*, 4, 14
- LoVerde M., Smith K. M., 2011, *JCAP*, 8, 3
- Maggiore M., Riotto A., 2010a, *ApJ*, 711, 907
- Maggiore M., Riotto A., 2010b, *ApJ*, 717, 515
- Maggiore M., Riotto A., 2010c, *ApJ*, 717, 526
- Maldacena J., 2003, *Journal of High Energy Physics*, 5, 13
- Mao Y., D'Aloisio A., Zhang J., Shapiro P. R., 2013, ArXiv e-prints
- Mao Y., Tegmark M., McQuinn M., Zaldarriaga M., Zahn O., 2008, *PRD*, 78, 023529
- Matarrese S., Verde L., 2008, *ApJ*, 677, L77
- Matarrese S., Verde L., Jimenez R., 2000, *ApJ*, 541, 10
- McQuinn M., Furlanetto S. R., Hernquist L., Zahn O., Zaldarriaga M., 2005, *ApJ*, 630, 643
- McQuinn M., Oh S. P., Faucher-Giguère C.-A., 2011, *ApJ*, 743, 82
- Mesinger A., Dijkstra M., 2008, *MNRAS*, 390, 1071
- Mo H. J., White S. D. M., 1996, *MNRAS*, 282, 347
- Musso M., Paranjape A., 2012, *MNRAS*, 420, 369
- Musso M., Paranjape A., Sheth R. K., 2012, ArXiv e-prints
- Musso M., Sheth R. K., 2012, *MNRAS*, 423, L102
- Namjoo M. H., Firouzjahi H., Sasaki M., 2013, *EPL (Europhysics Letters)*, 101, 39001
- Onken C. A., Miralda-Escudé J., 2004, *ApJ*, 610, 1
- Paranjape A., Lam T. Y., Sheth R. K., 2012, *MNRAS*, 420, 1429
- Paranjape A., Sheth R. K., 2012, *MNRAS*, 419, 132
- Pawlik A. H., Schaye J., van Scherpenzeel E., 2009, *MNRAS*, 394, 1812
- Robertson B. E., Furlanetto S. R., Schneider E., Charlot S., Ellis R. S., Stark D. P., McLure R. J., Dunlop J. S., Koekemoer A., Schenker M. A., Ouchi M., Ono Y., Curtis-Lake E., Rogers A. B., Bowler R. A. A., Cirasuolo M., 2013, ArXiv e-prints
- Ross A. J., Percival W. J., Carnero A., Zhao G.-b., Manera M., Raccanelli A., Aubourg E., Bizyaev D., et al. 2013, *MNRAS*, 428, 1116
- Salopek D. S., Bond J. R., 1990, *PRD*, 42, 3936
- Santos M. G., Ferramacho L., Silva M. B., Amblard A., Cooray A., 2010, *MNRAS*, 406, 2421
- Seery D., Lidsey J. E., 2005, *JCAP*, 6, 3
- Shapiro P. R., Giroux M. L., Babul A., 1994, *ApJ*, 427, 25
- Shapiro P. R., Iliev I. T., Raga A. C., 2004, *MNRAS*, 348, 753

Shapiro P. R., Mao Y., Iliev I. T., Mellema G., Datta K. K., Ahn K., Koda J., 2013, PRL, 110, 151301
 Shull J. M., Harness A., Trenti M., Smith B. D., 2012, ApJ, 747, 100
 Slosar A., Hirata C., Seljak U., Ho S., Padmanabhan N., 2008, JCAP, 8, 31
 Smith K. M., Ferraro S., LoVerde M., 2012, JCAP, 3, 32
 Sobacchi E., Mesinger A., 2013, ArXiv e-prints
 Tashiro H., Ho S., 2012, ArXiv e-prints
 Tashiro H., Sugiyama N., 2012, MNRAS, 420, 441
 Valageas P., 2010, A&A, 514, A46
 Verde L., Jimenez R., Kamionkowski M., Matarrese S., 2001, MNRAS, 325, 412
 Verde L., Wang L., Heavens A. F., Kamionkowski M., 2000, MNRAS, 313, 141
 Wang L., Kamionkowski M., 2000, PRD, 61, 063504
 Wyithe J. S. B., Cen R., 2007, ApJ, 659, 890
 Wyithe J. S. B., Loeb A., 2003, ApJ, 588, L69
 Wyithe J. S. B., Morales M. F., 2007, MNRAS, 379, 1647
 Xia J.-Q., Baccigalupi C., Matarrese S., Verde L., Viel M., 2011, JCAP, 8, 33
 Xia J.-Q., Bonaldi A., Baccigalupi C., De Zotti G., Matarrese S., Verde L., Viel M., 2010, JCAP, 8, 13
 Xia J.-Q., Viel M., Baccigalupi C., De Zotti G., Matarrese S., Verde L., 2010, ApJ, 717, L17
 Yokoyama S., Matsubara T., 2012, ArXiv e-prints
 Yoo J., 2010, PRD, 82, 083508
 Yoo J., Fitzpatrick A. L., Zaldarriaga M., 2009, PRD, 80, 083514
 Zhang J., Hui L., Haiman Z., 2007, MNRAS, 375, 324

APPENDIX A: DERIVATION OF THE NON-GAUSSIAN IONIZED DENSITY BIAS IN THE ESMR

In this appendix we present our derivation of the non-Gaussian ionized density bias from the ESMR. The first step is to compute the ionized fraction bias. We will then use equation (9) to convert the ionized fraction bias to the ionized density bias. We begin with the non-Gaussian ionized fraction contrast, equation (31), which contains both scale-independent and -dependent contributions. In what follows, we define the following functions for notational convenience:

$$\chi \equiv \frac{1}{3} \left\{ \frac{\delta_c - \delta_R}{S_{\min} - S_R} - \frac{1}{\delta_c - \delta_R} \right\}, \quad (\text{A1})$$

$$\psi \equiv \frac{1}{S_R} \left[\delta_c - (\delta_c - \delta_R) \coth \left(\frac{\delta_c^2 - \delta_c \delta_R}{S_R} \right) \right]. \quad (\text{A2})$$

A1 Scale-independent terms

The scale-independent contributions can be further divided into the Gaussian term and the non-Gaussian correction. The first term on the right-hand side of equation (31) yields the former. Taylor expanding it to first order about $\delta_R = 0$ and taking the limit as $S_R \rightarrow 0$ gives

$$b_x^G = \frac{2}{\delta_c} \frac{\partial \ln f_{\text{coll},0}^G}{\partial \ln S_{\min}}, \quad (\text{A3})$$

The non-Gaussian part comes from

$$\delta_x^{(i)} = \frac{\langle \delta_{\min}^3 \rangle}{f_{\text{coll},0}^G} \left(\frac{\partial f_{\text{coll}}^G}{\partial S_{\min}} \chi - \frac{f_{\text{coll}}^G}{f_{\text{coll},0}^G} \frac{\partial f_{\text{coll},0}^G}{\partial S_{\min}} \chi_0 \right), \quad (\text{A4})$$

where the “0” sub-script on χ again denotes the $\delta_R = 0$ and $S_R = 0$ limit. We Taylor expand $\delta_x^{(i)}$ to first order in δ_R about $\delta_R = 0$. The constant term is zero, while the linear term is

$$\delta_x^{(i)} = \frac{\langle \delta_{\min}^3 \rangle}{f_{\text{coll},0}^G} \left[\frac{\partial}{\partial \delta_R} \left(\chi \frac{\partial f_{\text{coll}}^G}{\partial S_{\min}} \right) \Big|_{\delta_R=0} - \frac{\chi_0}{f_{\text{coll},0}^G} \frac{\partial f_{\text{coll},0}^G}{\partial S_{\min}} \frac{\partial f_{\text{coll}}^G}{\partial \delta_R} \Big|_{\delta_R=0} \right] \delta_R. \quad (\text{A5})$$

Taking the limit as $S_R \rightarrow 0$ yields

$$\Delta b_x^{(i)} = -\frac{S_{\min}^{(3)}}{6} S_{\min} b_x^G \left[\frac{3\delta_c S_{\min} - \delta_c^3}{S_{\min}^2} + b_x^G \left(\frac{\delta_c^2}{S_{\min}} - 1 \right) \right], \quad (\text{A6})$$

where $S_{\min}^{(3)} \equiv \langle \delta_{\min}^3 \rangle / S_{\min}^2$ denotes the skewness of density fluctuations smoothed on the M_{\min} scale. As described in §2.3.1, this is the Lagrangian ionized fraction bias, which is equivalent to the Eulerian ionized fraction bias. We may therefore apply equation (9) to arrive at equation (32) for the scale-independent correction to the ionized density bias.

A2 The scale-dependent term

Scale-dependent contributions can come from sub-terms involving $\langle \delta_{\min}^2 \delta_R \rangle$ in the last term of equation (31). There are two such terms,

$$d_1 = \frac{\langle \delta_{\min}^2 \delta_R \rangle}{S_{\min}} \frac{1}{f_{\text{coll},0}^G} \frac{\partial f_{\text{coll}}^G}{\partial \ln S_{\min}} \psi, \quad (\text{A7})$$

and

$$d_2 = -3 \frac{\langle \delta_{\min}^2 \delta_R \rangle}{S_{\min}} \frac{1}{f_{\text{coll},0}^G} \frac{\partial f_{\text{coll}}^G}{\partial \ln S_{\min}} \chi. \quad (\text{A8})$$

Equation (31) is written in coordinate space whereas the scale-dependence of the bias is manifested in Fourier space. We employ a convenient method used by Desjacques et al. (2011b) for the conversion. Adapting their strategy to the current task, we take the cross-correlation, $\langle \delta_x \delta_R \rangle$, between the ionized fraction contrast and the large-scale smoothed density contrast. We then rearrange the equations to pick off the Fourier space bias parameter.

Desjacques et al. (2011b) considered the statistics of thresholded regions – regions in the initial density field with peak height above some given value. They showed that the power spectrum of thresholded regions, which in the Press-Schechter formalism can be interpreted as the collapsed fraction power spectrum, can to first order be expressed with a simple bias relation. Adopted to our notation, the linear bias relation they found is $\delta_{\text{fcoll}}(\mathbf{k}) = b_{\text{fcoll}}(k) \delta_{\min}(\mathbf{k})$. Noting that $\delta_{\text{fcoll}} = \delta_x$, and $b_{\text{fcoll}} = b_x$ in the ESMR, we can

write $\delta_x(\mathbf{k}) = b_x(k)\delta_{\min}(\mathbf{k})$. We use this relation to write the left-hand side of (31) as

$$\langle \delta_x \delta_R \rangle = \int \frac{d^3\mathbf{k}}{(2\pi)^3} b_x(k) \mathcal{M}_{\min}(k) \mathcal{M}_R(k) P_\phi(k). \quad (\text{A9})$$

If we can now rewrite the appropriate terms in the cross-correlation of δ_R with the right-hand side of (31) in a similar way, we can simply read off the bias coefficient.

Let us first consider equation (A7). We Taylor expand it to first order about $\delta_R = 0$, neglecting the constant term, since it will vanish upon taking the cross-correlation with δ_R . Taking the limit $S_R \rightarrow 0$, and using the property,

$$\lim_{S_R \rightarrow 0} \psi|_{\delta_R=0} = 0, \quad (\text{A10})$$

we can write the cross-correlation of d_1 with δ_R as

$$\langle d_1 \delta_R \rangle = \frac{\langle \delta_{\min}^2 \delta_R \rangle}{S_{\min}} \frac{\partial \ln f_{\text{coll},0}^G}{\partial \ln S_{\min}} \lim_{S_R \rightarrow 0} \left(\frac{\partial \psi}{\partial \delta_R} \Big|_{\delta_R=0} S_R \right) \quad (\text{A11})$$

Conveniently,

$$\lim_{S_R \rightarrow 0} \left(\frac{\partial \psi}{\partial \delta_R} \Big|_{\delta_R=0} S_R \right) = 1, \quad (\text{A12})$$

so

$$\langle d_1 \delta_R \rangle = \frac{\langle \delta_{\min}^2 \delta_R \rangle}{S_{\min}} \frac{\delta_c b_x^G}{2}. \quad (\text{A13})$$

In a similar manner it is straightforward to show that $\langle d_2 \delta_R \rangle = 0$.

The mixed correlator, $\langle \delta_{\min}^2 \delta_R \rangle$, can be written in a form similar to equation (A9) [see discussion leading up to equation (9) of D'Aloisio et al. (2012)],

$$\langle \delta_{\min}^2 \delta_R \rangle = \int \frac{d^3\mathbf{k}}{(2\pi)^3} \mathcal{M}_R(k, z) P_\phi(k) 4S_{\min} \mathcal{F}_{\min}^{(3)}(k). \quad (\text{A14})$$

Plugging this into equation (A13), in combination with equation (A9), yields

$$\Delta b_x^{(d)}(k) = 2\delta_c b_x^G \frac{\mathcal{F}_{\min}^{(3)}(k)}{\mathcal{M}_{\min}(k)}, \quad (\text{A15})$$

where the form factor $\mathcal{F}_{\min}^{(3)}(k)$ is defined in equation (34). We note that this expression is equivalent to equation (43) of Desjacques et al. (2011b) for $N = 3$. Their linear bias of thresholded regions is equivalent to our collapsed fraction bias, defined in equation (11). Since the ionized fraction bias is equivalent to the collapsed fraction bias in the ESMR, the former is also equivalent to the linear bias of thresholded regions in Desjacques et al. (2011b), hence the correspondence between their equation (43) and equation (A15). Finally, equations (9) and (A15) yield equation (33) for the scale-dependent correction to the ionized density bias.

APPENDIX B: DETAILS ON THE SOURCE EMISSIVITY IN THE LPTR

Here we derive expressions for the spatially averaged source emissivity and its first-order perturbation, which appear in equations (43) and (49) respectively. For convenience, we define the quantity $n_{\text{H, coll}}(\mathbf{r}, M_{\min}, R, \eta) \equiv n_{\text{H}}(\mathbf{r}, R, \eta) f_{\text{coll}}(M_{\min}, R, \delta_R, \eta)$, representing the density of hydrogen collapsed into ACHs, smoothed over scale R . Note that $n_{\text{H, coll}}$ appears in equation (40), and its time derivative appears in equation (39).

We write $n_{\text{H, coll}}$ in terms of a spatial average and a first-order perturbation as follows:

$$n_{\text{H, coll}}(\mathbf{r}, M_{\min}, R, \eta) = \bar{n}_{\text{H}} \left[f_{\text{coll},0}(M_{\min}, \eta) + \Delta_{\text{H, coll}}(\mathbf{r}, M_{\min}, R, \eta) \right]. \quad (\text{B1})$$

Referring back to equations (38), (39), and (40), the quantity ξ_s which appears in equation (43) can simply be read off from equation (B1); in source-model A, $\xi_s^A = \gamma^A(x_\nu) \partial [f_{\text{coll},0}(M_{\min}, \eta)] / \partial \eta$, while in source-model B, $\xi_s^B = \gamma^B(x_\nu) f_{\text{coll},0}(M_{\min}, \eta)$.

If we write the smoothed hydrogen number density as $n_{\text{H}}(\mathbf{r}, R, \eta) = \bar{n}_{\text{H}}(\eta) [1 + \delta_R(\mathbf{r}, \eta)]$, and the conditional collapsed fraction as $f_{\text{coll}}(M_{\min}, R, \delta_R, \eta) = f_{\text{coll},0}(M_{\min}, \eta) + \Delta f_{\text{coll}}(M_{\min}, R, \delta_R, \eta)$, then to leading order $\Delta_{\text{H, coll}} = \delta_R(\mathbf{r}, \eta) f_{\text{coll},0}(M_{\min}, \eta) + \Delta_{\text{fcoll}}(M_{\min}, R, \delta_R, \eta)$, and its Fourier transform is

$$\tilde{\Delta}_{\text{H, coll}}(\mathbf{k}, \eta) = f_{\text{coll},0}(\eta) \tilde{\delta}(\mathbf{k}, \eta) + \tilde{\Delta}_{\text{fcoll}}(\mathbf{k}, \eta), \quad (\text{B2})$$

where from here on we suppress the M_{\min} dependence for brevity (it should be understood that the collapsed fraction refers to the fraction of mass in halos above the ACH threshold), and the dependence on R has been dropped under the assumption of small k . The quantity $\tilde{\Delta}_{\text{fcoll}}$ may be written in terms of the collapsed fraction bias,

$$\tilde{\Delta}_{\text{fcoll}}(\mathbf{k}, \eta) = b_{\text{fcoll}}(\mathbf{k}, \eta) \tilde{\delta}(\mathbf{k}, \eta) f_{\text{coll},0}(\eta), \quad (\text{B3})$$

from which equation (B2) becomes

$$\tilde{\Delta}_{\text{H, coll}}(\mathbf{k}, \eta) = f_{\text{coll},0}(\eta) \left[1 + b_{\text{fcoll}}(\mathbf{k}, \eta) \right] \tilde{\delta}(\mathbf{k}, \eta). \quad (\text{B4})$$

The quantity $\tilde{\Delta}_s$ appearing in equation (49) can now be read off, yielding equations (53) and (54) in source-models A and B respectively.

The collapsed fraction bias parameters which enter these expressions follow trivially from the results of appendix A since, in the ESMR, the ionized fraction bias is assumed equal to the collapsed fraction bias. The Gaussian collapsed fraction bias is therefore equation (A3), while the scale-independent and -dependent terms from PNG are (A6) and (A15) respectively, each with the replacement $b_x \rightarrow b_{\text{fcoll}}$.